Comparison of different ocean tide models especially with respect to the GRACE satellite mission

Studienarbeit im Studiengang

Geodäsie und Geoinformatik

an der Universität Stuttgart

Bohan Wu

Stuttgart, February 2012

Pruefer: Prof.Dr.-Ing. Nico Sneeuw
Universität Stuttgart

Betreuer: Dr.-Ing. Matthias Weigelt
Universität Stuttgart

Erklärung der Urheberschaft

Ich erkläre hiermit an Eides statt, dass ich die vorliegende Arbeit ohne Hilfe Dritter und ohne Benutzung anderer als der angegebenen Hilfsmittel angefertigt habe; die aus fremden Quellen direkt oder indirekt übernommenen Gedanken sind als solche kenntlich gemacht. Die Arbeit wurde bisher in gleicher oder ähnlicher Form in keiner anderen Prüfungsbehörde vorgelegt und auch noch nicht veröffentlicht.

Ort, Datum   Unterschrift

Abstract

For the modeling of a static gravity field, the impact of ocean tides is subtracted from the GRACE data. Since there are more than one ocean tide model available, it is worth to learn the difference between the models and the consequence of applying different model. Three ocean tide models FES2004, EOT08a and EOT10a provided in the form of tidal maps are compared in this thesis. Based on the tidal maps, the disturbance in the potential and in the acceleration due to a single ocean tide is derived by using spherical harmonic analysis. Tools for visualization are developed to demonstrate the difference between the EOT models and FES2004 globally at a specific time point or locally at a specific site in a time period. Furthermore, a simulation of the GRACE mission and spherical harmonic analysis using the differential gravimetry approach build a closed loop simulation together, from which it can be find out, how the model difference affects the gravity field derived from GRACE data in the frequency domain.

Contents

List of Figures

List of Tables

Chapter 1

Introduction

The GRACE dual satellite mission offers the possibility of computing highly accurate gravity fields. Among the factors that influence its quality, the ocean tide model is one of the candidates. The effects due to ocean tides, which are the strongest short-period water mass redistribution in the Earth systems, are assumed known and could be removed from the gravity field by using a ocean tide model. Therefore, the quality of the ocean tide model has direct impact on the Earth gravity field derived from GRACE. Considering that the research work of GRACE data may use different ocean tide models, it is useful to investigate the model differences, in order to avoid wrongly interpretation of the model differences as apparent sea level variations or gravity variations.

The most well known ocean tide model in recent years, FES2004, taken as a reference model in GRACE gravity field modeling, is a combined product based on a hydrodynamic model. Among all the available global tide models, it has the highest resolution and is arguably most accurate.

In 2008, a new global ocean tide model, EOT08a was generated by German Geodetic Research Institute (DGFI) using an empirical analysis of harmonized and cross-calibrated multi-mission altimeter data acquired between October 1992 and October 2005 (Savcenko and Bosch, 2008). Besides the altimeter data of TOPEX, Poseidon, ERS-1 and ERS-2 mentioned previously, data from GFO, Jason-1 and ENVISAT are used in EOT08a. Two years later, EOT10a was derived as an update of EOT08a. The observation duration is extended to April 2010 and instead of altimeter of ERS-1 and GFO, data from Jason-2 is involved (Savcenko and Bosch, 2008).

The involved ocean tide models in this thesis are FES2004, EOT08a and EOT10a, which are all provided in the form of tidal maps. The main task of this thesis is to derive the disturbance in the potential and in the acceleration due to ocean tides based on the tidal maps of each tide model and to compare the potential difference between the models. It aims to identify the areas that show the model difference and the variation of the model difference over time. For a better understanding of the comparison result, tools for visualizing the model difference are developed, with which a specific single tide from each models can be compared and the result is interpreted in terms of geoid height. Furthermore, by a simulation of the GRACE mission and the developed analysis tool, one can find out how the model error affects the gravity field derived from GRACE data in the frequency domain.

The theoretical foundation of this thesis is introduced in Chapter 2. The mathematical formula are implemented in MATLAB for computing the disturbance in the potential and the accelerations due to ocean tides, for building the simulator and the corresponding analysis tool. Chapter 3 and Chapter 4 present the comparison results of the investigated ocean tide model. Since the disturbance in the potential due to ocean tides is not only a function of the observation position

but also the time point, we observe these two aspects separately to make the visualization work easier. Chapter 3 focuses on the global visualization of model difference at a certain time point. By setting the observation points on the earth surface it is achieved by a 2D graphic. Chapter 4 shows the timely variation of model difference at some certain point. In Chapter 5, a closed loop simulation is introduced and an example result of the implementation is shown.

Chapter 2

Theory of ocean tides analysis

This Chapter starts with an introduction of ocean tides and ocean tide modeling. Latter on, mathematical background of the computation from tidal maps to spherical harmonics and to the disturbance in the potential and acceleration will be discussed. Furthermore a simulator is built for the twin GRACE satellites to study to which extent the ocean tides impact the satellite motion. In the end, spherical harmonic analysis is performed to a simulated signal, which is composed of acceleration vectors generated by gravity field and a certain ocean tide model.

2.1 Ocean tides and ocean tide model

The Earth responses to the tide-generating potential (potential of celestial bodies) by means of various deformations, two of which are ocean tides and ocean-tide loading. The term ocean tides refers to the motion of the ocean surface (the relocation of water masses) relative to the seabed as a result of tide-generating forces. Ocean-tide loading is the deformation of the seabed and the mainland close to the coast as reaction to the effect of ocean tides. All deformations lead to a disturbance in the potential, which results in a direct disturbance in the acceleration at an observed space point, for instance a particular point in satellite orbit. It must be declared that the disturbance in the potential as well as disturbance in the acceleration discussed in this study are consequences of ocean tides and ocean-tide loading.

The reaction of the ocean to the tide-generating potential is described by frequency dependent tidal heights. With the assumption of ocean tides' linear behavior, every single one of them can not only be decoupled from all other tides, but also be handled separately without knowing the other tides. A single ocean tide $\zeta_s(\lambda, \phi, t)$, which is marked with the subscript s indicating a certain frequency, is expressed in terms of amplitude $\xi_s(\lambda, \phi)$ and phase $\delta_s(\lambda, \phi)$, in which (λ, ϕ) indicates geocentric longitude and latitude.

$$\zeta_s = \xi_s \cos(\theta_s + \chi - \delta_s) \tag{2.1}$$

In the equation above $\theta_s(t)$ represents the Doodson argument and χ the Doodson-Warburg phase bias. The Doodson argument (Doodson, 1921) of a certain ocean tide s is defined as a linear combination of the six classic Doodson elements (numerical value see (Simon et al., 1994)), τ, s, h, p, N' and P_s, which are invented to describe the position of the Sun and the Moon with respect to the Earth. Besides the six classic Doodson elements, elements that describe the position of other celestial bodies w.r.t the Earth are also used for argument calculation of the major tides today. However, the other celestial bodies are not considered in this thesis work, because the Sun and the Moon are the two main sources of generating ocean tides. The relative position of the

Sun and the Moon w.r.t. the Earth change all the time, so these six elements are time dependent. The Doodson numbers $d_{1,s}$, $d_{2,s}$, $d_{3,s}$, $d_{4,s}$, $d_{5,s}$ and $d_{6,s}$ are integer with values between 0 and 9. They are usually written as a six digits number which is unique for each tide. Since the six Doodson elements are time dependent with the reference epoch at 0:00 on 1st. January 2000, the Doodson argument $\theta_s(t)$ is a function of time and expressed as

$$\theta_s = d_{1,s}\tau + (d_{2,s} - 5)s + (d_{3,s} - 5)h + (d_{4,s} - 5)p + (d_{5,s} - 5)N' + (d_{6,s} - 5)P_s \qquad (2.2)$$

The value of Doodson-Warburg phase bias χ is frequency dependent (Dow, 1988). Details of the tides and the categories can be found in Tab. 3.2 and Chapter 3.2 and 3.4.

$$\chi = \begin{cases} 0 & \text{for semi diurnal and long period tide} \\ \frac{\pi}{2} & \text{for 165.555 tide namely K1 tide} \\ -\frac{\pi}{2} & \text{for diurnal tide except 165.555 tide} \end{cases}$$

Ocean tide models are distributed as two gridded maps for each major constituent (tide of main frequency). One is the map of the phase and the other one is the map of the quadrature amplitude of tide heights. Except the modelized major constituents, there are still many minor tides in the whole frequency spectrum of ocean tides. On one hand the absence of those minor tides in ocean tide models reduces the workload of modeling; on the other hand, it is hard to distinguish the minor tides and the major constituents from the observation data. In the light of the admittance theory (Marsh et al., 1987), the minor tides can be linear interpolated from major constituents. Although each minor tide plays only a small role, their total influence is significant. In spite of that, they are neglected in this thesis because of the small magnitude of their difference between models. Thus, the main subjects in this thesis are the major constituents.

2.2 Expansion of tide maps to spherical function

In the last section a single ocean tide $\zeta_s(\lambda, \phi, t)$ is described by a mathematical expression in Eq. 2.1. For convenience, the ocean tide can also be written in complex form as ζ_s^*.

$$\begin{aligned} \zeta_s^* &= \xi_s e^{i(\theta_s + \chi - \delta_s)} \\ &= (\xi_s \cos \delta_s - i\xi_s \sin \delta_s)e^{i(\theta_s + \chi)} \end{aligned} \qquad (2.3)$$

In the next step ζ_s^* is going to be expanded into spherical harmonic function [DOW,1988; textsc-GASOTTO, 1989], which is realized by the expansion of $\xi_s \cos \delta_s$ and $\xi_s \sin \delta_s$ to the maximum degree of N as shown in Eq. 2.4. $P_{lm}(\sin \phi)$ is the usual Legendre function of the first kind of degree l and order m . Afterwards the abbreviation P_{lm} will be used. The other parameters $(a_{lm,s}, b_{lm,s}, c_{lm,s}$ and $d_{lm,s})$ in both equations are spherical harmonic coefficients.

$$\begin{aligned} \xi_s \cos \delta_s &= \sum_{l=0}^{N} \sum_{m=0}^{l} (a_{lm,s} \cos m\lambda + b_{lm,s} \sin m\lambda) P_{lm}(\sin \phi) \\ \xi_s \sin \delta_s &= \sum_{l=0}^{N} \sum_{m=0}^{l} (c_{lm,s} \cos m\lambda + d_{lm,s} \sin m\lambda) P_{lm}(\sin \phi) \end{aligned} \qquad (2.4)$$

Substituting Eq. 2.4 into Eq. 2.3, the equation is rewritten as

$$\zeta_s^* = \sum_{l=0}^{N} \sum_{m=0}^{l} [(a_{lm,s} \cos m\lambda + b_{lm,s} \sin m\lambda) - i(c_{lm,s} \cos m\lambda + d_{lm,s} \sin m\lambda)] e^{i(\theta_s + \chi)} P_{lm}(\sin\phi) \quad (2.5)$$

The real part that we would like to focus on can be expressed as

$$\zeta_s = Re(\zeta_s^*) = \sum_{l=0}^{N} \sum_{m=0}^{l} [\frac{1}{2}(a_{lm,s} \mp d_{lm,s}) \cos(\theta_s + \chi \pm m\lambda) + \frac{1}{2}(c_{lm,s} \pm b_{lm,s}) \sin(\theta_s + \chi \pm m\lambda] P_{lm} \quad (2.6)$$

At this point ellipsoidal corrections (Balmino, 1995) are introduced. The increasing precision in measurement techniques today demands that ellipsoidal corrections should be applied to spherical harmonics considering that the tide models are described on the oblate shape of the Earth. The calculating process is given in Section 2.3 in detail. Distinguished from the coefficients without correction, the corrected coefficients are marked with asterisk, for example the term a_{lm}^* is used instead of a_{lm}. Now instead of Eq. 2.6 we have

$$\zeta_s = \sum_{l=0}^{N} \sum_{m=0}^{l} [\frac{1}{2}(a_{lm,s}^* \mp d_{lm,s}^*) \cos(\theta_s + \chi \pm m\lambda) + \frac{1}{2}(c_{lm,s}^* \pm b_{lm,s}^*) \sin(\theta_s + \chi \pm m\lambda] P_{lm} \quad (2.7)$$

Further, new terms which are linear combinations of the corrected spherical harmonic coefficients are introduced to simplify the writing.

$$\zeta_s = \sum_{l=0}^{N} \sum_{m=0}^{l} [C_{lm,s}^{\pm} \cos(\theta_s + \chi \pm m\lambda) + S_{lm,s}^{\pm} \sin(\theta_s + \chi \pm m\lambda] P_{lm} \quad (2.8)$$

with

$$C_{lm,s}^{\pm} = \frac{1}{2}(a_{lm,s}^* \mp d_{lm,s}^*) \qquad S_{lm,s}^{\pm} = \frac{1}{2}(a_{lm,s}^* \pm d_{lm,s}^*)$$

So far the coefficients $C_{lm,s}^{\pm}$ and $S_{lm,s}^{\pm}$ have been, just like the amplitude of tide heights, in the unit of length. It is known that the spherical harmonic coefficients should be dimensionless. Thus they are scaled by a dimension factor and converted by Eq. 2.9 to $\widehat{C}_{lm,s}^{\pm}$ and $\widehat{S}_{lm,s}^{\pm}$. The factor G is the gravitational constant (6.67428×10^{-11} m^{3}kg^{-1}s^{-2}), g_e means equatorial gravity (9.7803278 ms^{-2}) and ρ_w is the density of seawater (1025 kgm^{-3}).

$$\widehat{C}_{lm,s}^{\pm} = \frac{4\pi G \rho_w}{g_e(2l+1)} C_{lm,s}^{\pm} \qquad \widehat{S}_{lm,s}^{\pm} = \frac{4\pi G \rho_w}{g_e(2l+1)} S_{lm,s}^{\pm} \quad (2.9)$$

Then, Eq. 2.8 turns into Eq. 2.10

$$\zeta_s = \sum_{l=0}^{N} \sum_{m=0}^{l} [\widehat{C}_{lm,s}^{\pm} \cos(\theta_s + \chi \pm m\lambda) + \widehat{S}_{lm,s}^{\pm} \sin(\theta_s + \chi \pm m\lambda] P_{lm} \quad (2.10)$$

Performing the substitution again, the equation can be expressed in a simpler way as shown in Eq. 2.11.

$$\zeta_s = \sum_{l=0}^{N} \sum_{m=0}^{l} (\overline{C}_{lm,s} \cos(m\lambda) + \overline{S}_{lm,s} \sin(m\lambda)) P_{lm} \quad (2.11)$$

with

$$
\begin{aligned}
\overline{C}_{lm,s} &= \cos(\theta_s + \chi)(\widehat{C}_{lm,s}^+ + \widehat{C}_{lm,s}^-) + \sin(\theta_s + \chi)(\widehat{S}_{lm,s}^+ + \widehat{S}_{lm,s}^-) \\
\overline{S}_{lm,s} &= \cos(\theta_s + \chi)(\widehat{S}_{lm,s}^+ - \widehat{S}_{lm,s}^-) - \sin(\theta_s + \chi)(\widehat{C}_{lm,s}^+ - \widehat{C}_{lm,s}^-)
\end{aligned}
\tag{2.12}
$$

Now to exam the features of those coefficients, it is clear that time t is one of the variables in $\zeta_s(\lambda, \phi, t)$ and the footnote s means ζ_s is unique at different frequencies. The derivation process shows that the coefficients $\widehat{C}_{lm,s}^{\pm}$ and $\widehat{S}_{lm,s}^{\pm}$ in Eq. 2.10 are neither time dependent nor frequency dependent, but $\overline{C}_{lm,s}$ and $\overline{S}_{lm,s}$ are. Both of them contains the Doodson argument $\theta_s(t)$, which is a function of time, and Doodson-Warburg phase bias χ, which is frequency dependent.

2.3 Ellipsoidal correction to spherical harmonics

As a foundation of ocean tide models, it is assumed that the potential disturbance results from a surface layer of water masses coated on a ellipsoidal body. In the article "Ellipsoidal Corrections to Spherical Harmonics of Surface Phenomena Gravitational Effects" (Balmino, 1995), formulas are derived to the second order with respect to the flattening of the ellipsoid and the layer thickness. The computation of ellipsoidal corrections in this section is based on the algorithm described in the article, though adjustments are made to adapt it to the treatment of tidal maps.

The spherical harmonic analysis of the two components $\xi_s \cos \delta_s$ and $\xi_s \sin \delta_s$ in Eq. 2.3 generates two pairs of coefficients namely $(a_{lm,s}, b_{lm,s})$ and $(c_{lm,s}, d_{lm,s})$ in Eq. 2.4. Taken the first pair as an example, in Eq. 2.13 they are combined to one term h_{lm}, which is going to be frequently used in the calculation later.

$$
(2 - \delta_{lm})h_{lm} = a_{lm,s} - ib_{lm,s} \qquad \delta_{lm} = \begin{cases} 0, & l \neq m \\ 1, & l = m \end{cases}
\tag{2.13}
$$

To simplify the writing of the formulas later on, new terms are defined as follows:

$$
\varepsilon_2 = \frac{1}{2}e'^2 \qquad \varepsilon_4 = \frac{3}{8}e'^4
$$

with e' as the second eccentricity which is related to the first eccentricity by

$$
e'^2 = e^2/(1 - e^2)
$$

and

$$
\begin{aligned}
e_{lm} &= \frac{1}{2l+3}\left[\frac{(l-m+1)(l-m+2)}{2l+1}\frac{(l+m+1)(l+m+2)}{2l+5}\right]^{1/2} \\
f_{lm} &= \frac{2l(l+1) - 2m^2 - 1}{(2l-1)(2l+3)} \\
g_{lm} &= \frac{1}{2l-1}\left[\frac{(l-m)(l-m-1)}{2l-3}\frac{(l+m)(l+m-1)}{2l+1}\right]^{1/2}
\end{aligned}
$$

and

$$
\begin{aligned}
s_{lm} &= e_{lm}e_{l+2,m} \\
t_{lm} &= e_{lm}(f_{l+2,m} + f_{lm}) \\
u_{lm} &= e_{lm}g_{l+2,m} + f_{lm}^2 + e_{l-2,m}g_{lm} \\
v_{lm} &= g_{lm}(f_{lm} + f_{l-2,m}) \\
w_{lm} &= g_{lm}g_{l-2,m}
\end{aligned}
$$

The terms in the next block together build the ellipsoidal correction. They are expressed with the help of the definitions above. The value of R_e is given in Section 2.1. In this part, only the numerical relationship is given, in order to show the calculation process in this thesis. For more information about the physical meaning of the terms, please find in the article (Balmino, 1995).

$$
\begin{aligned}
\delta^1 K_{lm}^0 &= h_{lm} \\
\delta^1 K_{lm}^1 &= -(l+2)\varepsilon_2 \left[e_{l-2,m}h_{l-2,m} + f_{lm}h_{lm} + g_{l+2,m}h_{l+2,m}\right] \\
\delta^1 K_{lm}^2 &= \left[\frac{(l+1)(l+2)}{2}\varepsilon_2^2 + (l+2)\varepsilon_4\right] \\
&\quad \cdot \left[s_{l-4,m}h_{l-4,m} + t_{l-2,m}h_{l-2,m} + u_{lm}h_{lm} + v_{l+2,m}h_{l+2,m} + w_{l+4,m}h_{l+4,m}\right] \\
\delta^2 K_{lm}^0 &= \frac{1}{R_e}\frac{l+2}{2}h_{lm} \\
\delta^2 K_{lm}^1 &= -\frac{1}{R_e}(l+1)\varepsilon_2 \left[e_{l-2,m}h_{l-2,m} + f_{lm}h_{lm} + g_{l+2,m}h_{l+2,m}\right] \\
\delta^2 K_{lm}^2 &= \frac{1}{R_e}\left[\frac{l(l+1)}{2}\varepsilon_2^2 + (l+1)\varepsilon_4\right] \\
&\quad \cdot \left[s_{l-4,m}h_{l-4,m} + t_{l-2,m}h_{l-2,m} + u_{lm}h_{lm} + v_{l+2,m}h_{l+2,m} + w_{l+4,m}h_{l+4,m}\right]
\end{aligned}
$$

$$
K_{lm} = \delta^1 K_{lm}^0 + \delta^1 K_{lm}^1 + \delta^1 K_{lm}^2 + \delta^2 K_{lm}^0 + \delta^2 K_{lm}^1 + \delta^2 K_{lm}^2 \tag{2.14}
$$

It makes sense that the term $\delta^1 K_{lm}^0$ equals h_{lm} which is the combination of the coefficient pair $(a_{lm,s}, b_{lm,s})$, because the uncorrected spherical harmonic coefficients are derived under the condition that the earth's flattening is not taken into account. So in Eq. 2.14, the first term is the original state and the terms after it are actually the corrections

The last step is to return to the system of harmonic coefficient pair $(a_{lm,s}^*, b_{lm,s}^*)$. Obviously Eq. 2.13 and Eq. 2.15 share the same form but the equations are calculated in the opposite directions.

$$
a_{lm,s}^* - ib_{lm,s}^* = (2 - \delta_{lm})K_{lm} \tag{2.15}
$$

Obtaining $c_{lm,s}^*$ and $d_{lm,s}^*$ is achieved in the same way by inserting $c_{lm,s}$ and $d_{lm,s}$ into Eq. 2.13.

2.4 Potential and acceleration

To compare the ocean tide models, the tidal maps must be converted to physical quantities such as potential or acceleration. In general a geopotential field V at a certain point can be developed in spherical harmonic function. The disturbance in the gravitational potential due to a single ocean tide of frequency s at a point with spherical coordinate (ϕ, λ, r) exterior or on the surface of the Earth can be expressed as

$$V_s^{tide}(\phi, \lambda, r) = \frac{GM}{R_e} \sum_{l=0}^{n} \sum_{m=0}^{l} \left(\frac{R_e}{r}\right)^{l+1} (\overline{C}_{lm,s} \cos m\lambda + \overline{S}_{lm,s} \sin m\lambda) P_{lm}(\sin\phi) \qquad (2.16)$$

Here GM is geocentric gravitational constant ($3.986004418 \times 10^{14} \mathrm{4\,m^3 s^{-2}}$), R_e the equatorial radius of the Earth (6378136.6 m), $P_{lm}(\sin\phi)$ the usual Legendre function of the first kind of degree l and order m. The potential is determined up to degree and order of n which must be not larger than the maximum degree and order of the spherical harmonic expansion N in Eq. 2.4. Comparing equation Eq. 2.16 and Eq. 2.11, it is obvious that the solid spherical harmonic function of potential field has an upward continuation term which depends on degree l and the dimensioning is performed by the constant factor GM/R_e.

It should be noted that V_s^{tide} is only part of the total disturbance in the potential, because so far the ocean-tide loading has not been considered. The ocean tides redistribute water mass with respect to land and the Earth as a whole responses to external forces caused by this process as an elastic body. The effect as result is described as the ocean-tide loading. To make the model more accurate, it should be taken into account. The disturbance in the potential due to ocean-tide loading $V_s^{loading}$ are computed in different ways according to the data type in each model. For more information about the dataset offered by the ocean tide models please see Chapter 3.1.

Since Model FES2004 has no loading tidal maps, following the description in the IERS Conventions, the load deformation coefficient (LOVE number) k_l' of degree l are adopted for the calculation. In Eq. 2.17 we see that $V_s^{loading}$ is actually a fraction of V_s^{tide} with the load deformation coefficient as factor (Casotto, 1989).

$$V_s^{loading}(\phi, \lambda, r) = k_l' V_s^{tide}(\phi, \lambda, r) \qquad (2.17)$$

in which $k_2' = -0.3075$, $k_3' = -0.195$, $k_4' = -0.132$, $k_5' = -0.1032$, $k_5' = -0.0892$, for the rest degree $k_l' = 0$.

The models ETO08a and EOT10a provide besides tidal maps also the corresponding loading tidal maps. Since both types of maps share the same data structure, for tide s $V_s^{loading}$ is obtained by going through the steps from Eq. 2.4 to Eq. 2.16 with the data from loading tidal map instead of the tidal map as well.

In summary the disturbance in the potential at point (ϕ, λ, r) caused by tide s is the total effect of two types of deformation.

$$V_s(\phi, \lambda, r) = V_s^{tide}(\phi, \lambda, r) + V_s^{loading}(\phi, \lambda, r) \qquad (2.18)$$

The disturbance in the potential at point (ϕ, λ, r) generated by tides from several frequencies is the sum of single tides.

$$V(\phi, \lambda, r) = \sum_s V_s(\phi, \lambda, r) \qquad (2.19)$$

The disturbance in the potential can be also interpreted by using geoid height following the Bruns formula $N = \frac{T}{\gamma}$, in which N, T and γ stand for geoid height, gravity potential and gravity constant respectively. In the case of this thesis γ takes the value of mean equatorial gravity $g_e = 9.7803278 \, \text{ms}^{-2}$.

The vector on the left panel below is the partial derivation of a potential in the local spherical coordinates system (LSCS) whose physical meaning is acceleration. If the potential refers to a particular point in satellite orbit for instance, the acceleration vector can be transformed to the Earth-fixed Cartesian system (E) by using the rotation matrix given in Eq. 2.20. So the acceleration vector in the Earth-fixed Cartesian system is equals to $\mathbf{R}^E_{LSCS} \nabla V$.

$$\nabla V = \begin{pmatrix} \frac{\partial V}{\partial r} \\ \frac{1}{r}\frac{\partial V}{\partial \phi} \\ \frac{1}{r\cos\phi}\frac{\partial V}{\partial \lambda} \end{pmatrix} \qquad \mathbf{R}^E_{LSCS} = \begin{pmatrix} \cos\phi\cos\lambda & -\sin\phi\cos\lambda & -\sin\lambda \\ \cos\phi\sin\lambda & -\sin\phi\sin\lambda & \cos\lambda \\ \sin\phi & \cos\phi & 0 \end{pmatrix} \qquad (2.20)$$

Taken the potential in Eq. 2.16 as an example, the partial derivatives can be written explicitly in the following form.

$$\begin{aligned} \frac{\partial V^{tide}_s}{\partial r} &= -\frac{GM}{r^2} \sum_{l=0}^{n} \sum_{m=0}^{l} (l+1) \left(\frac{R_e}{r}\right)^l (\overline{C}_{lm,s} \cos m\lambda + \overline{S}_{lm,s} \sin m\lambda) P_{lm} \\ \frac{1}{r}\frac{\partial V^{tide}_s}{\partial \phi} &= \frac{GM}{r^2} \sum_{l=0}^{n} \sum_{m=0}^{l} \left(\frac{R_e}{r}\right)^l (\overline{C}_{lm,s} \cos m\lambda + \overline{S}_{lm,s} \sin m\lambda) \frac{\partial P_{lm}}{\partial \phi} \\ \frac{1}{r\cos\phi}\frac{\partial V^{tide}_s}{\partial \lambda} &= \frac{GM}{r^2} \sum_{l=0}^{n} \sum_{m=0}^{l} \frac{m}{\cos\phi} \left(\frac{R_e}{r}\right)^l (\overline{S}_{lm,s} \cos m\lambda - \overline{C}_{lm,s} \sin m\lambda) P_{lm} \end{aligned} \qquad (2.21)$$

Owing to the linearity in Eq. 2.18 and Eq. 2.19, the acceleration vector at point (ϕ, λ, r) caused by a tide of frequency s is expressed as

$$\nabla V_s(\phi, \lambda, r) = \mathbf{R}^E_{LSCS}[\nabla V^{tide}_s(\phi, \lambda, r) + \nabla V^{loading}_s(\phi, \lambda, r)] \qquad (2.22)$$

and the acceleration vector at the same point generated by tides from several frequencies is expressed as

$$\nabla V(\phi, \lambda, r) = \sum_s \nabla V_s(\phi, \lambda, r) \qquad (2.23)$$

2.5 Orbit simulation and spherical harmonic analysis

2.5.1 Orbit simulation

A satellite's position and its velocity can be determined by six Keplerian elements a, e, i, Ω, ω and M_0.

- Semimajor axis a: the sum of the periapsis and apoapsis distances divided by two.

- Eccentricity e: shape of the ellipse, describing how flattened it is compared with a circle.

- Inclination i: vertical tilt of the ellipse w.r.t. the reference plane, measured at the ascending node

- Right ascension of the ascending node Ω: horizontally orients the ascending node of the ellipse w.r.t the reference frame's vernal point

- Argument of perigee ω: the angle measured from the ascending node to the semimajor axis

- Mean anomaly at the reference epoch M_0: position of the orbiting body along the ellipse at epoch t_0

The mean motion $n = \sqrt{\frac{GM}{a^3}}$ enables the calculation of the mean anomaly

$$M = n \cdot (t - t_0) + M_0 \tag{2.24}$$

The value of GM is given in Section 2.4. After iteratively determining of the eccentric anomaly E by equation

$$E = M + e \cdot \sin E \tag{2.25}$$

The position vector $\mathbf{x}_o$ in orbit system can be described by the true anomaly ν and orbit radius r with the knowledge from Eq. 2.26 and Eq. 2.27. The subscript o represents the orbit coordinates system, i means the inertial coordinates system and e is the Earth-fixed coordinates system.

$$\mathbf{x}_o = [r \cos \nu \quad r \sin \nu \quad 0] \tag{2.26}$$

with

$$\cos \nu = \frac{\cos E - e}{1 - e \cdot \cos E} \qquad \sin \nu = \frac{\sqrt{1 - e^2} \sin E}{1 - e \cdot \cos E} \qquad r = \frac{a(1 - e^2)}{1 + e \cdot \cos \nu} \tag{2.27}$$

or in a simpler way

$$\mathbf{x}_o = \left[a(\cos E - e) \quad a\sqrt{1 - e^2} \sin E \quad 0 \right] \tag{2.28}$$

The velocity vector is the first derivation of the position vector in time. With the knowledge

$$\frac{dE}{dt} = \frac{1}{1 - e \cos E} \frac{dM}{dt} = \frac{n}{1 - e \cos E} \tag{2.29}$$

we get

$$\mathbf{v}_o = \frac{d\mathbf{x}_o}{dt} = \left[\frac{-na \sin E}{1 - e \cos E} \quad \frac{na\sqrt{1 - e^2} \cos E}{1 - e \cos E} \quad 0 \right] \tag{2.30}$$

Both the position vector and the velocity vector can be transformed from the orbit coordinates system into inertial coordinates system by using Eq. 2.31, in which $\mathbf{R}_3$ is the rotation matrix with respect to z-axis and $\mathbf{R}_1$ to x-axis.

$$\mathbf{x}_i = \mathbf{R}_3(-\Omega)\mathbf{R}_1(-i)\mathbf{R}_3(-\omega)\mathbf{x}_o \tag{2.31}$$

Further, they can also be transformed into the Earth-fixed coordinate system and converted into spherical coordinates.

$$\mathbf{x}_e = \mathbf{R}_3(GAST)\mathbf{x}_i \tag{2.32}$$

where GAST stands for Greenwich Apparent Sidereal Time, and with apparent right ascensions referred to the equinox. It should be mentioned that precession, nutation and polar motion are neglected here.

2.5.2 Spherical harmonic analysis

The spherical harmonic analysis is achieved by using the differential gravimetry approach. The subscript A and B in the formulas later indicate two satellites respectively. The core principle of this analysis, as presented in Eq. 2.33, is the relative gradient projected on the line-of-sight vector. Explanation of the symbols are offered in the following paragraphs.

$$(\nabla V_B - \nabla V_A)\mathbf{e}_{AB} = \nabla V_B^{r\phi\lambda}\mathbf{e}_B^{r\phi\lambda} - \nabla V_A^{r\phi\lambda}\mathbf{e}_A^{r\phi\lambda} \tag{2.33}$$

On the right hand side of Eq. 2.33, ∇V_B and ∇V_A refer to the partial derivatives of potential at satellite B and A respectively and the symbol $\mathbf{e}_{AB}$ stands for the line-of-sight unit vector between satellite A and B in inertial system. On the right hand side of Eq. 2.33, the components are in local system of the two satellites respectively. The equal sign can be applied in Eq. 2.33 because the result in both coordinate systems is a scalar. The explicit expressions of $\nabla V_B^{r\phi\lambda}$ and $\nabla V_A^{r\phi\lambda}$ originated from Eq. 2.20 and Eq. 2.21 in spherical coordinates of the Earth-fixed system (r_B, ϕ_B, λ_B) and (r_A, ϕ_A, λ_A) separately. The notations $\mathbf{e}_B^{r\phi\lambda}$ and $\mathbf{e}_A^{r\phi\lambda}$ represent that the line of sight unit vector $\mathbf{e}_{AB}$ in the LSCS is evaluated at the location of satellites B and A.

Since the rotation matrix of the Earth-fixed Cartesian system to the LSCS $\mathbf{R}_{LSCS}^E$, given in Eq. 2.20, depends on the position of the satellite, the transformation needs to be evaluated for each satellite separately.

$$\mathbf{e}_B^{r\phi\lambda} = \mathbf{R}_{LSCS}^E(r_B, \phi_B, \lambda_B)\mathbf{R}_3(GAST)\mathbf{e}_{AB} \tag{2.34}$$

$$\mathbf{e}_A^{r\phi\lambda} = \mathbf{R}_{LSCS}^E(r_A, \phi_A, \lambda_A)\mathbf{R}_3(GAST)\mathbf{e}_{AB} \tag{2.35}$$

Therefore, Eq. 2.33 can be expressed as Eq. 2.36

$$
\begin{aligned}
(\nabla V_B - \nabla V_A)\mathbf{e}_{AB} =\ & \frac{\partial V}{\partial r}e_B^r - \frac{\partial V}{\partial r}e_A^r + \frac{1}{r_B}\frac{\partial V}{\partial \phi}e_B^\phi - \frac{1}{r_A}\frac{\partial V}{\partial \phi}e_A^\phi \\
& + \frac{1}{r_B\cos\phi_B}\frac{\partial V}{\partial \lambda}e_B^\lambda - \frac{1}{r_A\cos\phi_A}\frac{\partial V}{\partial \lambda}e_A^\lambda
\end{aligned} \tag{2.36}
$$

in which

$$\mathbf{e}^{r\phi\lambda} = \begin{bmatrix} e^r & e^\phi & e^\lambda \end{bmatrix} \tag{2.37}$$

Since the values of the components on the left hand side of Eq. 2.36 can be acquired through measurement, they build the observation vector $\mathbf{l}$. On the right hand side of Eq. 2.36, the

spherical harmonic coefficients $\overline{C}_{lm,s}$ and $\overline{S}_{lm,s}$, which are unknown parameters, can be written explicitly to build the vector $\mathbf{x}$, with the help of Eq. 2.21. Further the explicit entries for the design matrix $\mathbf{A}$ can be derived as well. It is worth mentioning that the position of a specific element depends on the maximum degree L of the spherical harmonic expansion and the ordering of coefficients. This is neglected here for simplicity.

For $\overline{C}_{lm,s}$ coefficients:

$$
\begin{aligned}
a_{ij} &= -\frac{GM}{r_B^2}(l+1)(\frac{R_e}{r_B})^l P_{lm}^B \cos(m\lambda_B)e_B^r + \frac{GM}{r_A^2}(l+1)(\frac{R_e}{r_A})^l P_{lm}^A \cos(m\lambda_A)e_A^r \\
&+ \frac{GM}{r_B^2}(\frac{R_e}{r_B})^l \frac{\partial P_{lm}^B}{\partial \phi}\cos(m\lambda_B)e_B^\phi - \frac{GM}{r_A^2}(\frac{R_e}{r_A})^l \frac{\partial P_{lm}^A}{\partial \phi}\cos(m\lambda_A)e_A^\phi \\
&- \frac{GM}{r_B^2}(\frac{R_e}{r_B})^l \frac{m}{\cos\phi_B}P_{lm}^B \sin(m\lambda_B)e_B^\lambda + \frac{GM}{r_A^2}(\frac{R_e}{r_A})^l \frac{m}{\cos\phi_A}P_{lm}^A \sin(m\lambda_A)e_A^\lambda
\end{aligned}
\tag{2.38}
$$

For $\overline{S}_{lm,s}$ coefficients:

$$
\begin{aligned}
a_{ij} &= -\frac{GM}{r_B^2}(l+1)(\frac{R_e}{r_B})^l P_{lm}^B \sin(m\lambda_B)e_B^r + \frac{GM}{r_A^2}(l+1)(\frac{R_e}{r_A})^l P_{lm}^A \sin(m\lambda_A)e_A^r \\
&+ \frac{GM}{r_B^2}(\frac{R_e}{r_B})^l \frac{\partial P_{lm}^B}{\partial \phi}\sin(m\lambda_B)e_B^\phi - \frac{GM}{r_A^2}(\frac{R_e}{r_A})^l \frac{\partial P_{lm}^A}{\partial \phi}\sin(m\lambda_A)e_A^\phi \\
&- \frac{GM}{r_B^2}(\frac{R_e}{r_B})^l \frac{m}{\cos\phi_B}P_{lm}^B \cos(m\lambda_B)e_B^\lambda + \frac{GM}{r_A^2}(\frac{R_e}{r_A})^l \frac{m}{\cos\phi_A}P_{lm}^A \cos(m\lambda_A)e_A^\lambda
\end{aligned}
\tag{2.39}
$$

According to the classic form for applying least squares adjustment, we reform Eq. 2.36 into matrix form.

$$
\mathbf{l} = \mathbf{A}\mathbf{x} \tag{2.40}
$$

The result of the least squares adjustment follows

$$
\mathbf{x} = (\mathbf{A}^T\mathbf{A})^T\mathbf{A}\mathbf{l} \tag{2.41}
$$

Chapter 3

Global visualization of the model differences

The theoretical foundation of how to deal with tidal maps and calculate disturbance in the potential was provided from Section 2.1 to 2.3. In this Chapter the potential difference between models are interpreted and compared in measure of geoid height with the help of global visualization. The first part of this chapter introduces the data set in each model. To make the comparison later easier, one of the models is chosen as the reference model. The comparison of each constituent from different models comes in the following 3 Sections, which are divided on the basis of tide period, since the model differences of constituents with similar frequency have some features in common.

According to the previos knownledge in Chapter 2, it is known that the potential of ocean tides varies over time. The potential difference between ocean tidal models, therefore, is also a function of time. During the investigation, the model differences in a period of time are globaly visualized. However, it is hard to show the time feature within 2-dimensional graphics of the Earth. Hence the main task of this chapter is only to identify the locations with distinct model difference and to gain a sense of the extent, to which the models differ from each other. The timely model difference will be discussed in chapter 4.

In this chapter, graphics are chosen as typical examples of potential difference at a certain time point. The color bar in the images for each constituent are unified, so that the comparison between models can be directly perceived. All the potential difference are calculated at the height of 6378146 m from the Earth center.

3.1 Data set and reference model

All in all, three ocean tidal models, FES2004, EOT08a and EOT10, are investigated in this these work. It must be mentioned that the data set of FES2004 model has two versions, one of which is presented directly as spherical harmonic coefficient delivered from IERS. The other one is provided in form of tidal maps just like EOT08a and EOT10a model. The data offered by FES2004 are in two different forms, but theoretically they ought to represent the same model. As a mater of fact the coefficients derived from the tidal maps after the instructions in Chapter 2 are not identical to the coefficients offered by IERS. Hence the two types of Data of FES2004 are treated as individuals, whose names are distinguished by the suffix "IERS" in brackets.

| Name	Data Source	Data Type
FES2004(IERS)	IERS Conventions	spherical harmonic coefficients
FES2004	IERS Conventions	tidal maps
EOT08a	Savcenko R. and W. Bosch (2008)	tidal maps and loading tidal maps
EOT10a	Savcenko R. and W. Bosch (2010)	tidal maps and loading tidal maps

Table 3.1: *Models used for comparison*

While the harmonic coefficients and tidal maps of 19 major constituents are provided in FES2004(IERS) and FES2004, the other models only offered as tidal maps of certain constituents. Tab. 3.2 below offers an overview of the available tidal maps in each model. Only 15 constituents are listed here. The rest 4 constituents contained in FES2004(IERS) are Om1, Om2, Sa and Ssa, whose periods cover range from semiannual to several years. Since for some constituents the tidal maps are not available from the EOT models, the EOT models adopt the corresponding tidal maps from FES2004 for those constituents, when we calculate the total potential of these 19 constituents.

| Tide	Period [d]	EOT08a	EOT10a	FES2004
Mm	27.56	-	√	√
Mf	13.66	-	√	√
Mtm	9.13	-	-	√
Msqm	7.096	-	-	√
Q1	1.1195	√	√	√
O1	1.0758	√	√	√
P1	1.0027	√	√	√
K1	0.9973	√	√	√
S1		-	√	√
2N2	0.5377	√	√	√
N2	0.5274	√	√	√
M2	0.5175	√	√	√
S2	0.5000	√	√	√
K2	0.4986	√	√	√
M4	0.2587	√	√	√

Table 3.2: *Available tidal maps in the EOT models and FES2004*

According to the degree of development in IERS Conventions the FES2004(IERS) were computed up to degree and order 100, so this accuracy is maintained for spherical harmonic expansion of the tidal maps and loading tidal maps. Considering that FES2004 provides tidal map for single constituent like the EOT models, FES2004 is chosen as reference. What we observed in this thesis, is the difference between models. By using the tidal maps, three models are treated in the same process. Therefore, after the subtraction systematic effects will be cancel. All the comparisons made later in this chapter are based on the potential of one of the EOT model minus FES2004 presented in measure of geoid height. The way of potential converted to geoid length is told in the section 2.4.

Fig. 3.1 and Fig. 3.2 provide an impression of total potential difference, namely the sum of potential difference of 19 major constituents, between models at 12:00 UTC on 10. January 2000. Overall Fig. 3.1 and Fig. 3.2 show similar patterns except that one has an positive extreme spot in the northern Hudson Bay (the Foxe Basin) but the other one has negative extreme values along the Canadian St. Lawrence River. As the images have the same color bar, it is not difficult to notice that EOT10a resembles FES2004 a little bit more than EOT08a, at least at this time point. It should be mentioned that although there are signals in the river area near the estuary but the signals are normally not strong. It is unlikely that the great model difference occurs there. Later it is also proved by the producer of the EOT models (Savcenko and Bosch, 2008) that EOT10a has error at St.Lawrence River.
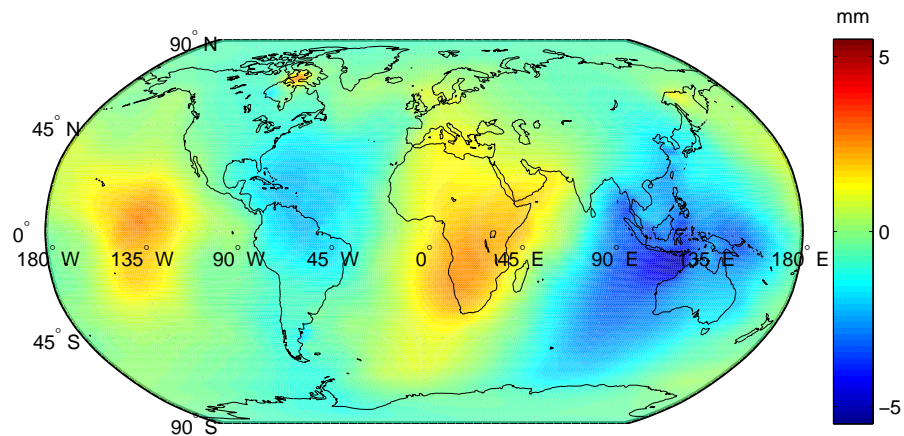
Figure 3.1: *Total potential difference between EOT08a and FES2004 in terms of geoid height,12:00 UTC on 10.Jan.2001*
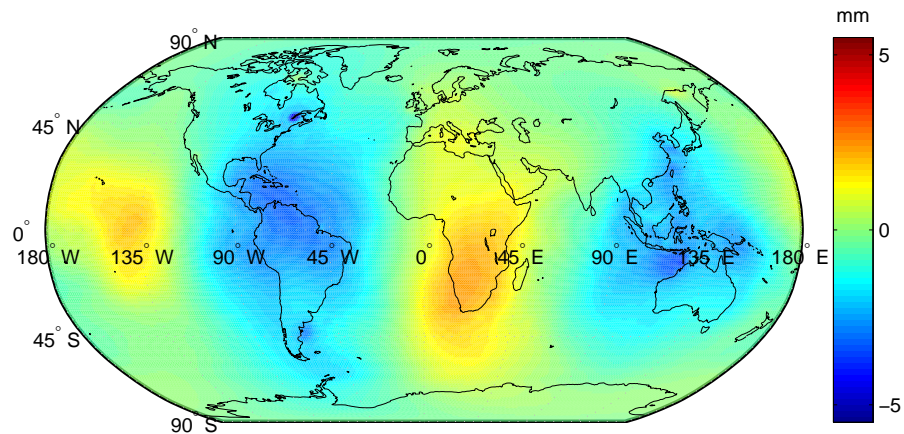
Figure 3.2: *Total potential difference between EOT10a and FES2004 in terms of geoid height,12:00 UTC on 10.Jan.2000*

In both images, 4 large patterns appear along the equator. Although the patterns are not regular oval, we can clearly tell that the positive and negative value occur in turn. According to the feature of the spherical harmonic coefficients, the connection between the graphic and the coefficients of degree l order m can be build. The number of the transition points between positive and negative extreme in longitude equals to $2m$, while the number of the transition

points between positive and negative extreme in latitude equals to $l - m$. From the irregular patterns in Fig. 3.1 and Fig. 3.2 we can tell that the model difference distributes in many different frequency, but the most dominant one is $\overline{C}_{22}$ and $\overline{S}_{22}$.

3.2 long period constituents

The investigated long period tides include Mm, Mf, Mtm and MSqm (see Tab. 3.2). Due to the lack of tidal maps in the EOT models, EOT08a is completely excluded from the comparison and EOT10a only takes part in the comparison of Mm and Mf with FES2004. So the situation here is very simple, which is explained by the table below with the main features of the model difference.

Tide	EOT08a - FES2004	EOT10a - FES2004
Mm	-	Zonal stripes with extreme spot near the equator
Mf	-	max. difference < 0.6 mm
Mtm	-	-
Msqm	-	-

Table 3.3: *Overview of the model difference at long period constituents*

Since the potential difference of tide Mm and Mf between ETO10a and FES2004 share most of the features, only the images of tide Mf are illustrated here. As demonstrated in Fig. 3.3, there are horizontal stripes on the globle map and spots in the ocean region lined up on the equator. From the image, it is not easy to tell spherical hamonic coefficients of which degree and order dominate the model difference. It is certain that the main factors are the coefficients of low frequency.
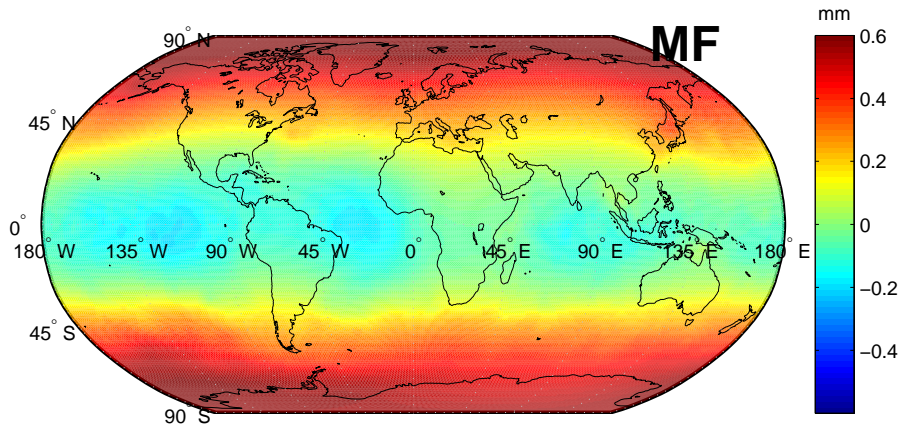
Figure 3.3: *Potential difference of Mf tide between EOT10a and FES2004 in terms of geoid height,12:00 UTC on 10.Jan.2000*

3.3 Diurnal constituents

The investigated diurnal tides include Q1, O1, P1, K1 and S1 (See Tab. 3.2). The small S1 tide is cause by diurnal atmospheric presser loading. Since its excitation is unlike any other diurnal tides, it is quite unique in this constituent group. The other tides share several common features such as four large scale patterns in each quadrant of the potential difference graphic and extremes with the same sign are usually in the diagonal quadrants.

Tab. 3.4 provides an over view of the magnitude of the potential difference between models. The maxim values listed here may not coincide with them from the illustrations later in this section, because the graphics can only show the situation at a certain time point, but at this point the global maximum may not occur. The maximum difference of the two EOT models with respect to FES2004 is almost the same.

Tide	Q1	O1	P1	K1
global maximum [mm geoid]	0.6	2	1	2.5

Table 3.4: *Magnitude of the global maximum difference between the EOT models and FES2004 for diurnal constituents*

In Fig. 3.4 the two pairs of extremes with round and clear edge center clockwise on the Pacific Ocean southeast of Japan, the Indian Ocean southwest of Australia, Patagonia and the Pacific southwest of the United States. In comparison the most noticeable feature of Fig. 3.5 is the blurry boundary of the anomalous patterns instead of clean-cut contour line. The extremes appear roughly in the same location but the with different magnitude. From the patterns it can be ... that the most model difference reflects on the spherical harmonic coefficient $\overline{C}_{21}$ and $\overline{S}_{21}$.
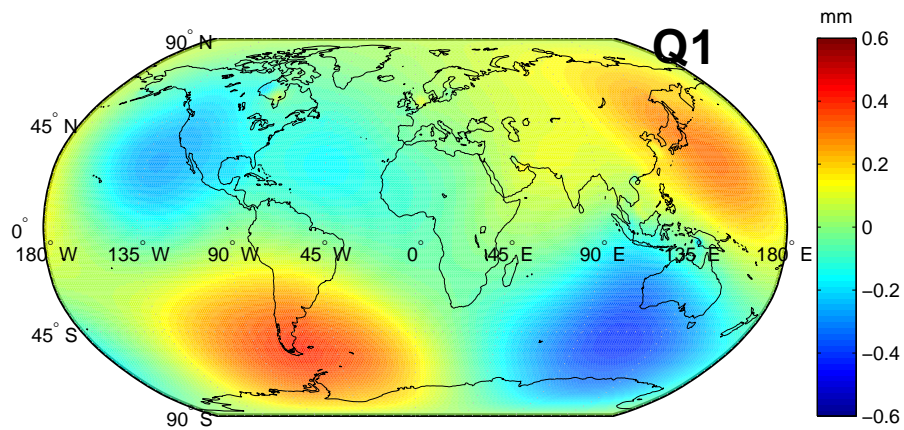
Figure 3.4: *Potential difference of Q1 tide between EOT08a and FES2004 in terms of geoid height,12:00 UTC on 10.Jan.2000*

For O1 tide, the images for potential difference between the EOT models and FES2004 are not presented here, since both images resemble Fig. 3.4 every much. The form and the location of the patterns are very similar. The only difference is that the extreme has a magnitude of 2 mm in term of geoid height in both images of O1 tide.
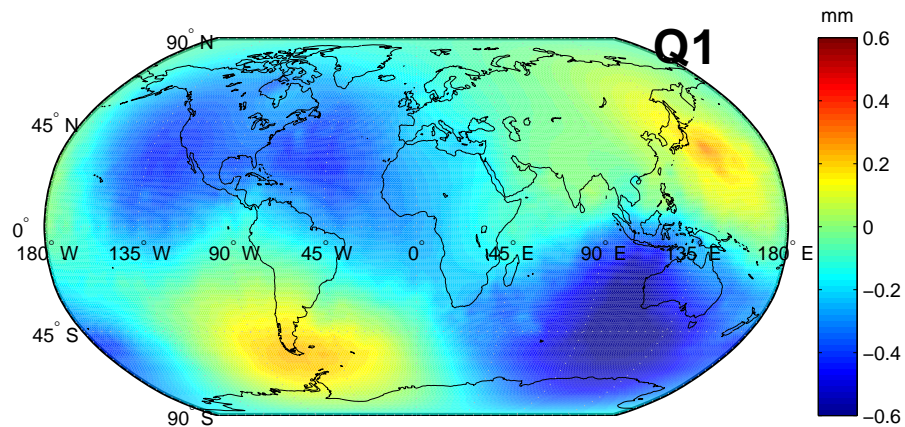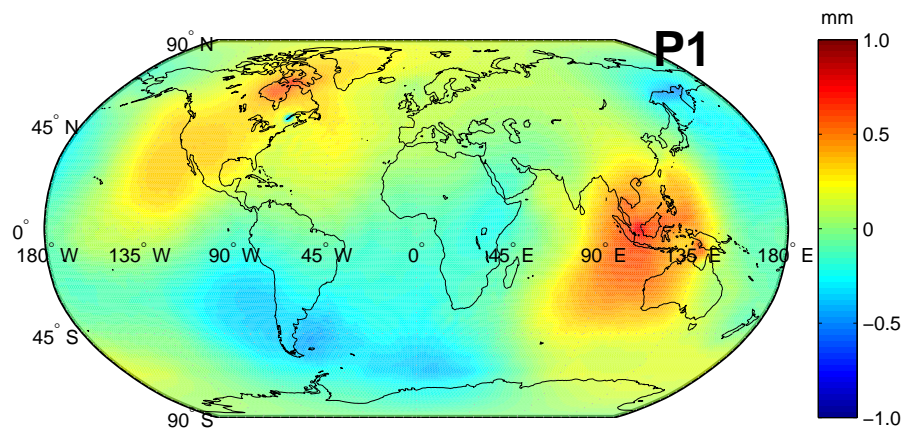
Figure 3.5: *Potential difference of Q1 tide between EOT10a and FES2004 in terms of geoid height,12:00 UTC on 10.Jan.2000*

Fig. 3.6 and Fig. 3.7 demonstrate the model difference for P1 tide. In Fig. 3.6 one of the pattern with maximum covers the whole North Atlantic, the Hudson Bay and the Baffin Bay and extends to the Mediterranean Sea and the Gulf of Mexico. Another large positive patch covers the eastern half of the Indian Ocean, the South China Sea and the whole Indonesia Sea. The two negative patterns are located in the North Pacific Ocean together with the Sea of Okhotsk and the Atlantic Ocean between South America and Africa respectively. The global maximum emerges in the sea southeast of Singapore. In addition a yellow spot in the Arabian Sea also attracts the attention.
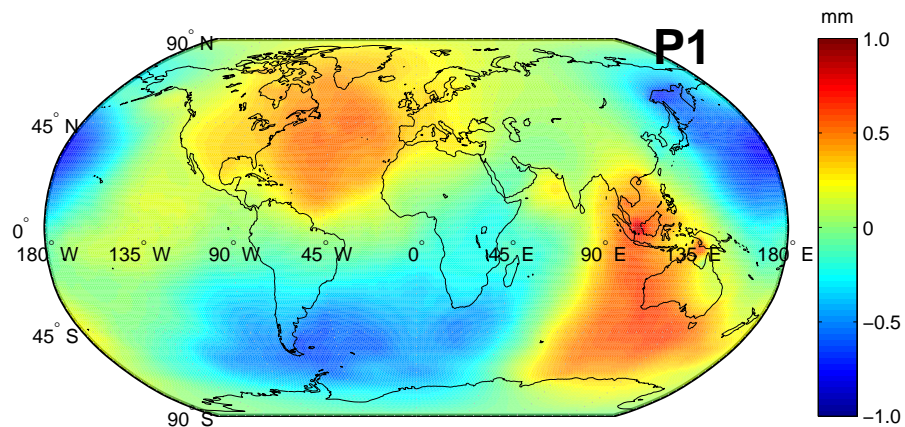
Figure 3.6: *Potential difference of P1 tide between EOT08a and FES2004 in terms of geoid height,12:00 UTC on 10.Jan.2000*

Fig. 3.7 shows that EOT10a differs from FES2004 mainly in the Hudson Bay and the pattern extends through North America to the Pacific Ocean southwest of the Unites States. It is easy to be noticed that among the positive difference on the North America Plate a negative spot emerges along the Canadian St. Lawrence River. The other negative differences are in the Sea of Okhotsk near the coastline of Russia and in the ocean around the southern South America. Although we can roughly recognize the four large patches with extreme values, it is not that easy

Figure 3.7: *Potential difference of P1 tide between EOT10a and FES2004 in terms of geoid height,12:00 UTC on 10.Jan.2000*

to connect the potential difference to the spherical harmonic coefficients of a specific degree and order.

For K1 tide, Fig 3.8 presents the potential difference between EOT08a and FES2004. The image for model EOT10a and FES2004 is omitted, because it is almost the same as Fig 3.8. The form, the location and the color of the patterns are nearly the same. So as the magnitude of the extreme values. Compared to the other diurnal tides, K1 tide has the largest potential difference between models. New phenomena emerge in the potential difference graphic of K1. Instead of four large patterns, it shows six separate regions with extreme values. The most notable one is that model difference up to 1 mm of geoid height occurs in the northwest Indian Ocean, south of the Arabian Sea, in the Read Sea and the Persian Gulf. Distinct model difference in this area appears for the first time as we go through the investigation previous in this chapter.
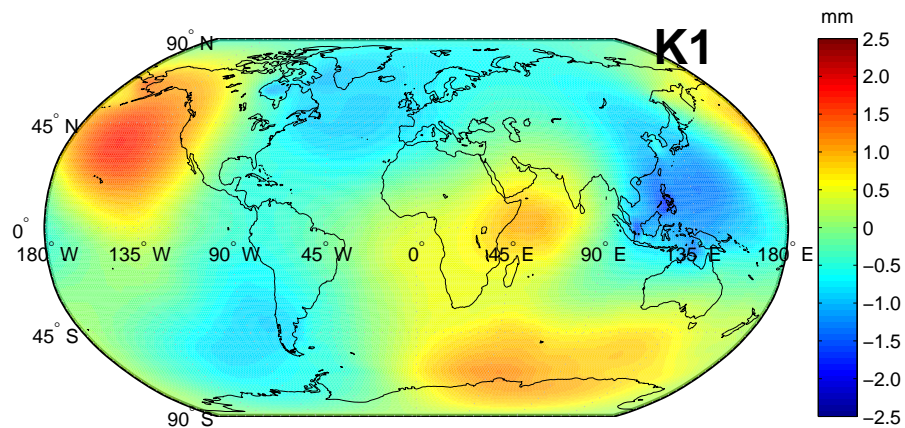
Figure 3.8: *Potential difference of K1 tide between EOT08a and FES2004 in terms of geoid height,12:00 UTC on 10.Jan.2000*

3.4 Semidiurnal constituents

The investigated semidiurnal tides include 2N2, N2, M2, S2 and K2 (See Tab. 3.2). M2 and S2, caused directly by the moon and the sun, are the most dominant tide in all these major constituents. The total potential difference between the EOT models and FES2004 (See Fig. 3.1 and Fig. 3.2) appear to be dominated by the M2 and S2 tide. 2N2 is rather a weak tide and from the table below it can be seen that its potential differences between the EOT models and FES2004 are quite small.

	Tide	2N2	N2	M2	S2	K2
global maximum	EOT08a-FES2004	0.2	1	4	5	1
[mm geoid]	EOT10a-FES2004	0.2	1	4	15	1

Table 3.5: *Magnitude of the global maximum difference between the EOT models and FES2004 for semidiurnal constituents*

For M2 tide, the potential difference between EOT08a and FES2004 is shown in Fig. 3.9. Large scale patterns emerge in the equatorial Pacific Ocean, in the equatorial Atlantic Ocean, in the Indian Ocean and the South China Sea. Positive and negative extremes occur alternately, two of which are in the Pacific Ocean. Although the form of the four patterns are not regular, it can be clearly recognized that they line up along the equator. Similar to Fig 3.1 told at the end of Section 3.1, the model difference reflects mostly on the coefficients $\overline{C}_{22}$ and $\overline{S}_{22}$.

The potential difference of M2 tide between EOT08a and FES2004 looks much the same as Fig. 3.9 with the only difference that the maximum in the north Hudson Bay vanishes. Thus, the graphic is omitted.
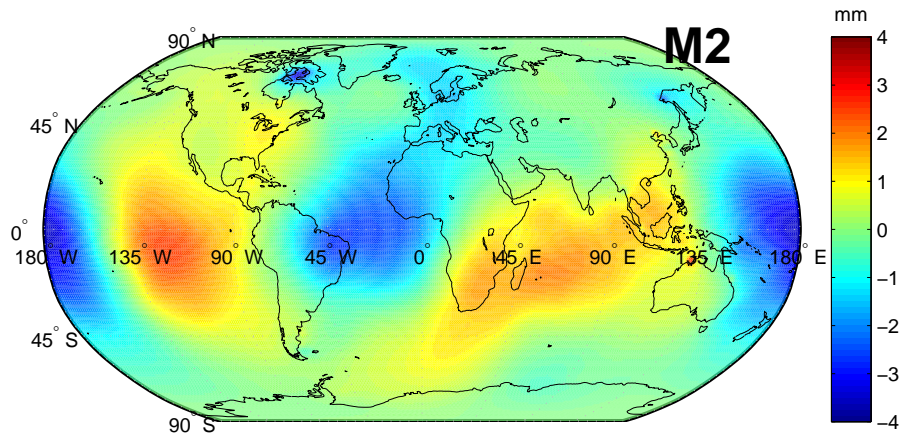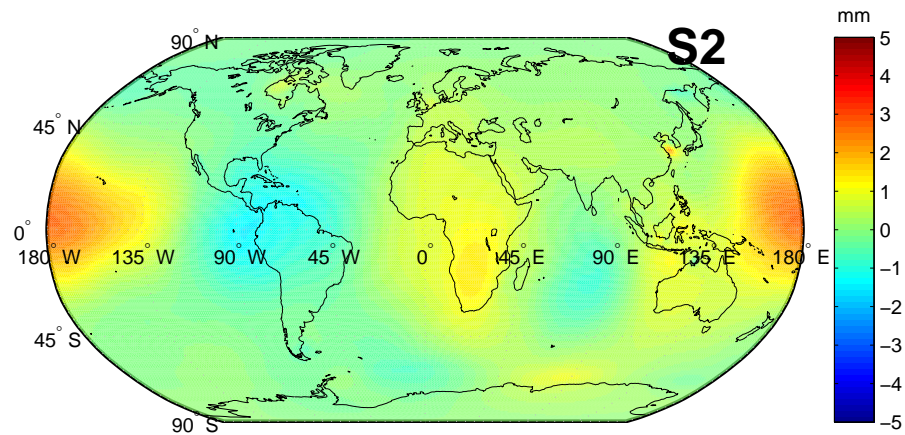

Figure 3.9: *Potential difference of M2 tide between EOT08a and FES2004 in terms of geoid height,12:00 UTC on 10.Jan.2000*

Furthermore, there are also small patches around the Great Lakes, in the north Hudson Bay and in the Sea of Okhotsk close to the Russian coast. That the extreme in the north Hudson Bay (the Foxe Basin) has the value around 4 mm in terms of geoid height offers the proof that the model difference in this region is contributed mainly by M2 tide.More to be noticed is that a red spot with the value of approximately 2.5 mm in geoid height stands out in the Joseph Bonaparte

Gulf of Australia. The pattern in the Atlantic extends further to the Greenland Sea covering the west part of the Mediterranean Sea,the North Sea and the Baltic Sea.

The two graphics of potential difference for N2 tide is omitted here, since they are very similar to M2 only with color bar of different magnitude. For N2 tide, EOT10a has only slight difference to FES2004 in the north Hudson Bay, which can be hardly recognized. N2 tide also shows distinct difference between EOT08a and FES2004 in this region, as M2 tide does,but with a smaller magnitude of 1 mm in terms of geoid height.
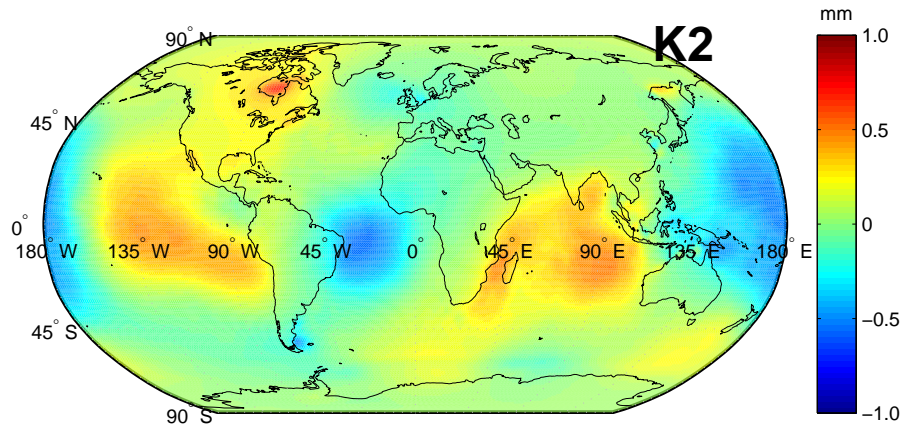

Figure 3.10: *Potential difference of S2 tide between EOT08a and FES2004 in terms of geoid height,12:00 UTC on 10.Jan.2000*
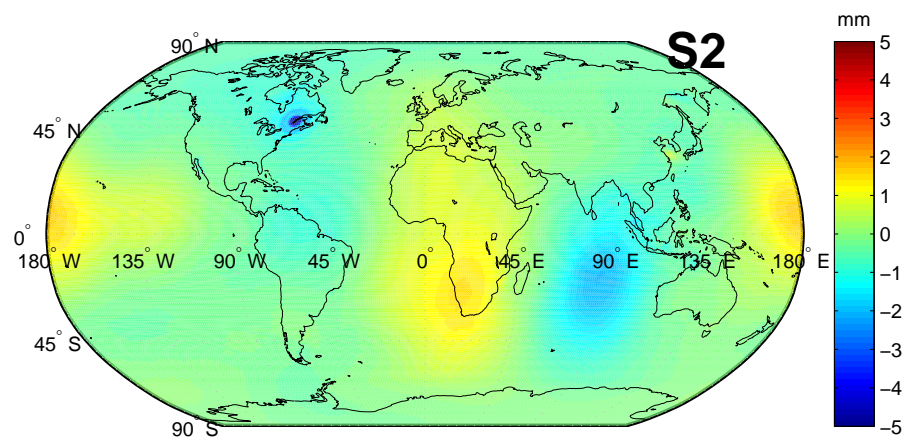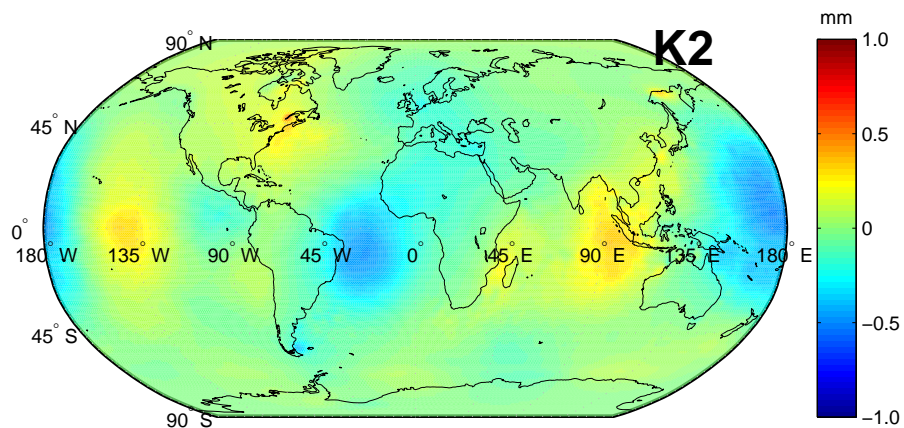

Figure 3.11: *Potential difference of S2 tide between EOT10a and FES2004 in terms of geoid height,12:00 UTC on 10.Jan.2000*

Regarding S2 tide, the most prominent feature is that EOT10a is very different from FES2004 in the area with the Canadian St. Lawrence River in the center. At the time point of Fig. 3.11, the extreme value at this place does not reach the maximum, which can reach more than 15 mm in terms of geoid height. More details about the potential difference at this place can be fund in Section 4.1.2. In Fig. 3.11, patterns are visible in the equatorial Pacific Ocean, in the Indian Ocean and in the water near southern Africa.

In Fig. 3.10, EOT08a differs from FES2004 in the Pacific northwest of South America and the Caribbean Sea, in the Atlantic Ocean and the Indian Ocean close to the Antarctica. In the Yellow Sea, there is a red spot with the value about 3 mm in terms of geoid height. Comparing Fig. 3.10 and Fig. 3.11, it is obvious that the extreme value in the Pacific Ocean is much smaller in Fig. 3.11.

Figure 3.12: *Potential difference of K2 tide between EOT08a and FES2004 in terms of geoid height,12:00 UTC on 10.Jan.2000*

Figure 3.13: *Potential difference of K2 tide between EOT10a and FES2004 in terms of geoid height,12:00 UTC on 10.Jan.2000*

Similar to the graphics of M2, Fig. 3.12 shows patterns in the equatorial Pacific Ocean, in the equatorial Atlantic Ocean, in the Indian Ocean and in the Bay of Bengal. The patterns of K2 and the continental margin fit into each other more neatly than any other constituents previously in this Chapter did. The most noticeable differences in small areas are in the Hudson Bay with geoid height value of about 0.7 mm as well as at the Patagonian Shelf with geoid height value of about 0.6 mm. There are also small patches scattered in the Yellow Sea, in the Sea of Okhotsk close to the Russian coast, in the Gulf of Mexico, in the Sea close to the northeast coastline of United States, in the South China Sea and the Banda Sea. Not far from the Antarctica coastline, positive and negative patterns appear in turns.

Comparing Fig. 3.13 to Fig. 3.12, there is no extreme values in the Hudson Bay but in the area with the Canadian St. Lawrence River in the center. The size of the large patterns with positive value in the Pacific Ocean and the Indian Ocean is significantly reduced. EOT10a has apparently smaller difference to FES2004 regarding K2 tide.

3.5 Quarter-diurnal constituent

In all the major constituents investigated in this theses work, M4 which also belongs to the group of shallow water tides, is the only quarter-diurnal constituent. In shallow water the dynamics become nonlinear and the tide frequency spectrum appears more complicated (**?**). Not until recent years did it become possible to resolve shallow water tides from other major constituents. M4 is the tide that is caused by the nonlinear distortions of M2 in shallow water.

Compared with the major constituents in other period groups, large changes take place in the graphic of potential difference between models. Large scale patterns that occur all the time in the graphics of constituents previously talked about do not exist in and Fig. 3.15. All the model differences locate either on the water or in coastal regions. The most notable places in Fig. 3.14 are the dark red spot in the Gulf of Guinea and in the Pacific Ocean as the global maximum. M4 shows clear difference on the northwest European shelf, for it is generated by the dominant M2 tide whose potential difference between models is also strong in this region. In the Hudson Bay and the Patagonian shelf the models show again distinct difference. Close to the lands around the Indian Ocean and around the Atlantic Ocean, small areas with opposite color turn up in turn. This phenomenon can also be seen in the south Atlantic and the south Indian Ocean observed in east and west direction.

In general EOT10a has potential difference from FES2004 less than 0.2 mm in geoid height. The scattered small spots in Fig. 3.14 have much smaller value but can still be recognized in spite of the vague impression. In Fig. 3.15 the positive maximum locates in the Pacific Ocean. The two negative maximum lie in the Bering Sea and the Atlantic Ocean south of Brazil. The rest other spots are located at the estuary of the Amazon River, at the Patagonian shelf, in the sea on the south of UK and the sea on the west of France.
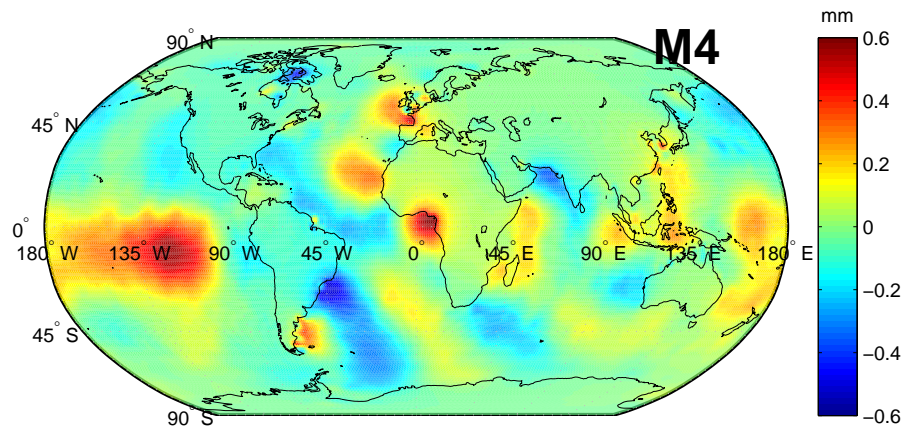
Figure 3.14: *Potential difference of M4 tide between EOT08a and FES2004 in terms of geoid height,12:00 UTC on 10.Jan.2000*
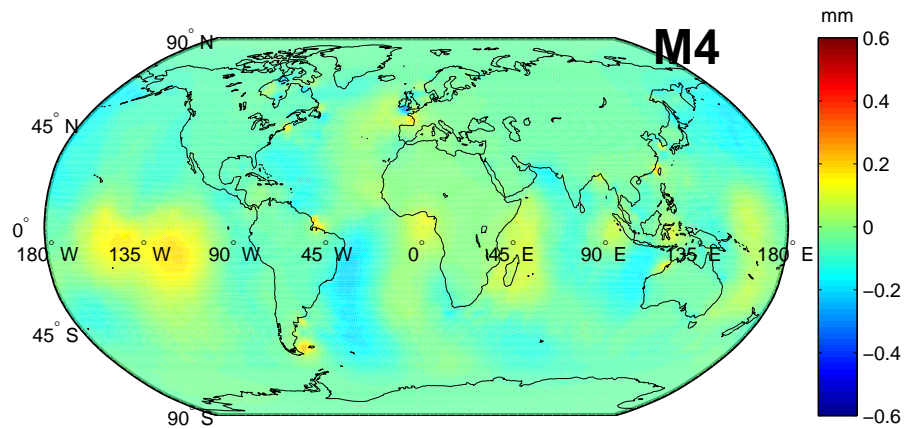
Figure 3.15: *Potential difference of M4 tide between EOT10a and FES2004 in terms of geoid height,12:00 UTC on 10.Jan.2000*

Chapter 4

Local visualization of the model differences

In the last chapter, many locations are identified with distinct potential difference between models. Some of them have been mentioned very often, such as the Hudson Bay, the Canadian St. Lawrence River, the South China Sea, etc. In this chapter we focus on the time aspect of potential difference. It is realized by observing the potential difference at a specific point with the height of 6378146 m from the earth center in a period of time. For each chosen location, the potential difference due to the major constituents as well as the total potential differences are investigated. Furthermore, the first derivative of the potential namely the acceleration at the given point is computed. Both the absolute acceleration from each model and the acceleration difference between models are presented as well.

All together 30 places are picked out over the world as the interesting areas for this these work. The chosen places are listed in the Appendix A with coordinates of longitude and latitude.

The graphics in this chapter always display the time dimension in the X-axis. The zero point means the start of the observation and from the scale marks represent the number of hours or days after the start time. For the diurnal tide the time period is set as 36 hours and for the semidiurnal tide 18 hours. K1, the strongest tide in the diurnal tide group, as well as the dominant M2 and S2 are illustrated each time for a chosen place. The superposition of all the diurnal constituents except S1, the semidiurnal and the quarter-diurnal constituents in this study is also graphically presented with a time span of 30 days to show the total potential difference between models.

4.1 The Foxe Basin and the St. Lawrence River Valley

The model difference at the Foxe Basin and the St. Lawrence River Vally show the most prominent features. These two places have been identified by the first two graphics of Chapter 3 (See Fig. 3.1 and Fig. 3.2).

4.1.1 The Foxe Basin

The Foxe Basin is in the Canadian territory, on the north of the Hudson Bay. They are connected by the Foxe Channel. The largest potential difference in the Foxe Basin occurs between EOT08a and FES2004 in M2. Fig. 4.1 illustrates the potential difference of M2 in this area at interval of 3 hours. These images coincide with the situation presented in Fig. 4.1.
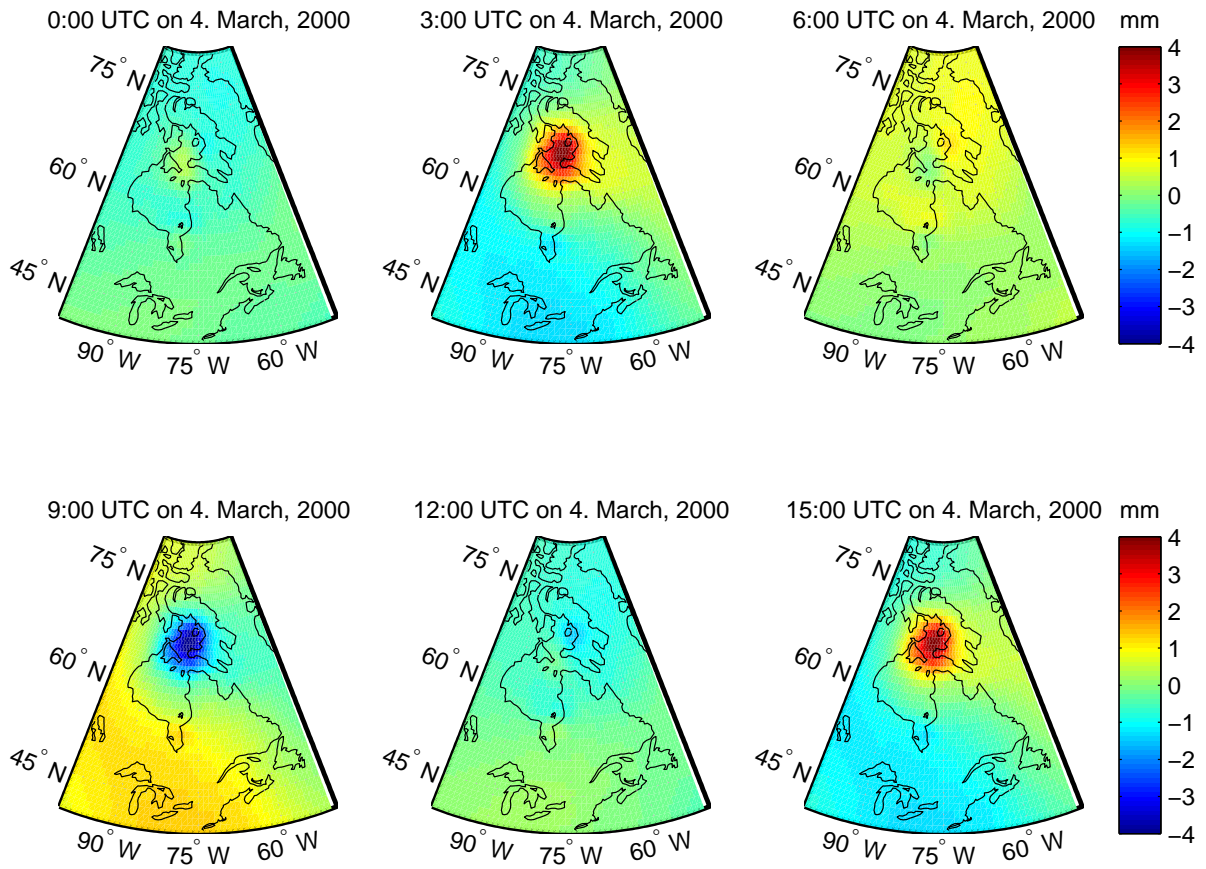
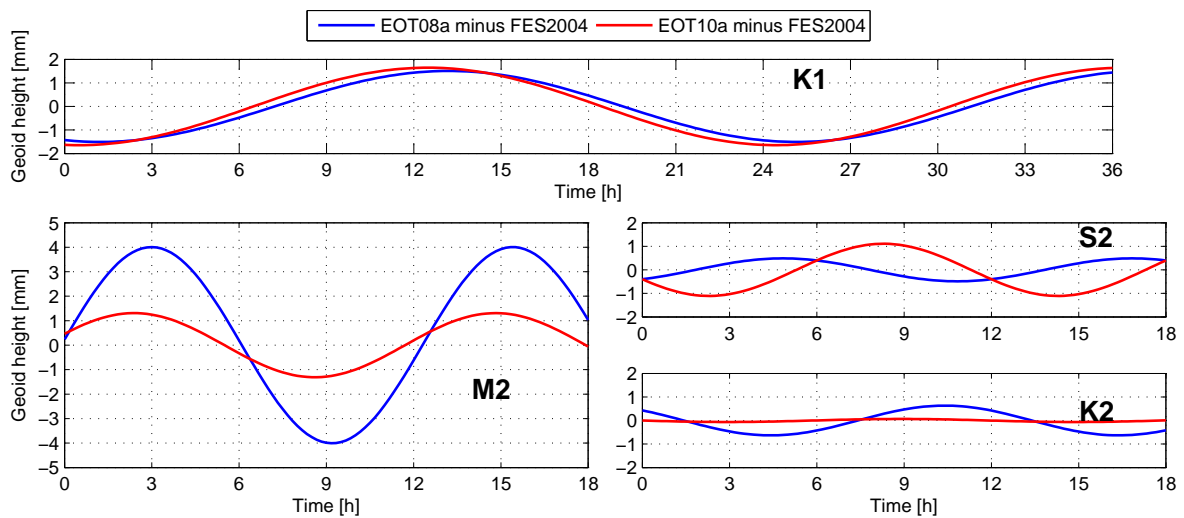**Figure 4.1:** *Potential difference of M2 between EOT08a and FES2004 in geoid height, the Foxe Basin*


Figure 4.2: *Potential difference of single constituent at $65°N\ 80°W$, start time 00:00 UTC on 4. March, 2000*

The graphics of four single constituents reveal the variation of model difference over time, which resemble a sinusoidal behavior with the period of the constituent, whose period conforms to the period of the corresponding constituent. Here the M2 tide shows strong potential difference between EOT08a and FES2004 with the maximum value exceeding 4 mm in geoid height. On the contrary the curve of EOT10a minus FES2004 in the chart of M2 has much smaller amplitude of about 1 mm. In the other three charts the amplitudes are all less than 2 mm. The EOT10a resembles FES2004 very much at the K2 tide. Slight phase shift can be identified at K1 and M2 and it is clearly visible at S2.

The superposition of the potential difference of the major constituents mentioned at the beginning of this chapter generates a complicated structure, whose data of 30 days are presented in Fig 4.3. In the graphic, that the peaks of the two curves appeal very often not at the same time, indicates slight phase shift between EOT08a and EOT10a. However, the graphic shows mostly that they have different amplitude. From observing the local maximum it is fund that EOT08a differs from FES2004 at most about 2 mm in geoid height more than EOT10a does. EOT10a differs from FES2004 not more than 5 mm in geoid height.
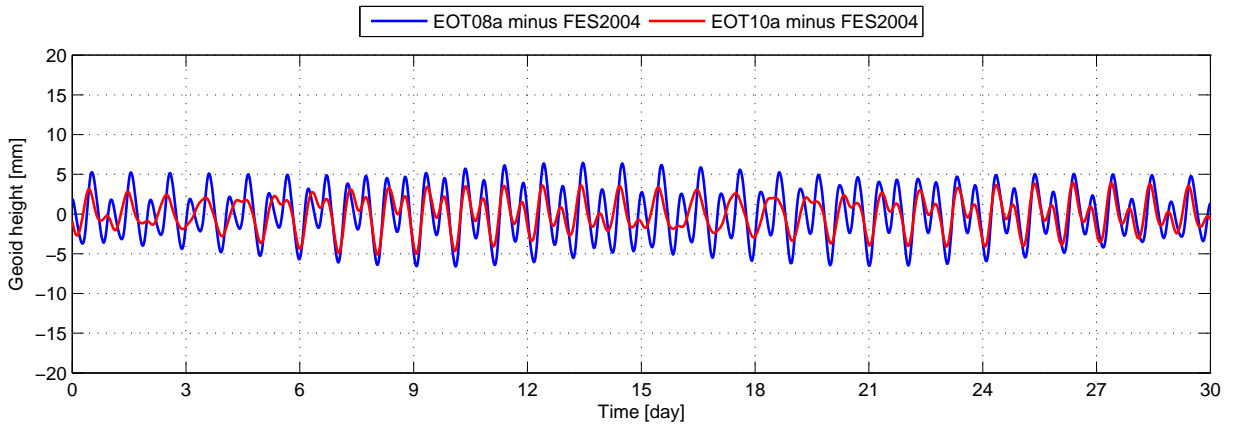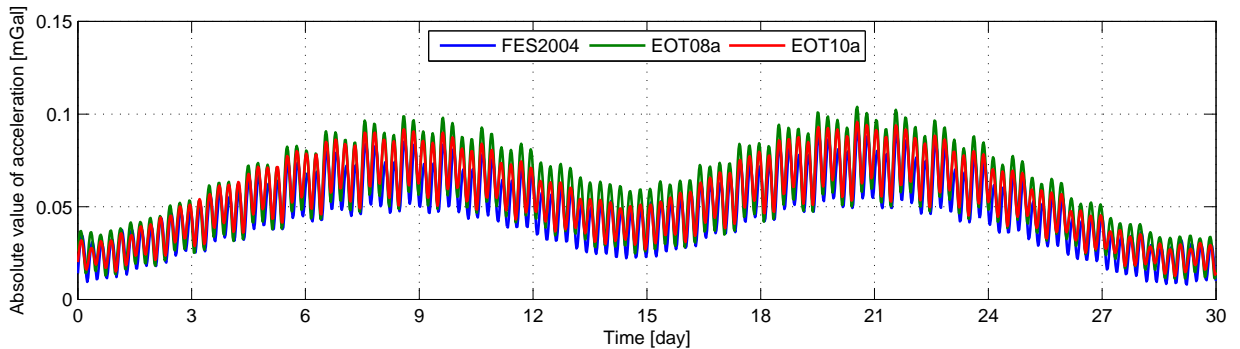

**Figure 4.3:** *Total potential difference at $65°N\ 80°W$, start time 00:00 UTC on 1. March, 2000*
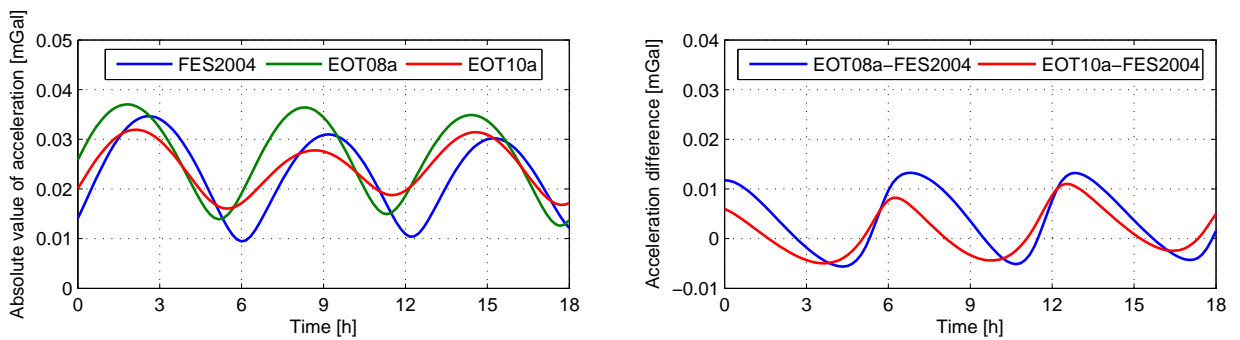
Figure 4.4: *Absolute value of accelerations and acceleration differences at $65°N\ 80°W$, start time 00:00 UTC on 1st March, 2000*

Fig. 4.4 illustrates both the absolute value of accelerations and their difference in a short time period, while Fig. 4.5 and Fig. 4.6 provides a impression of them in 30 days. All the accelerations are derived from the corresponding total potential in Fig. 4.3. In Fig. 4.4, phase shift and difference in amplitude are both clearly visible.

In the left panel of Fig.4.5, we see that the absolute value of accelerations are between 0.01 and 0.11 mGal. Their form resemble a sinusoidal behavior. The largest acceleration belongs to EOT10a and the smallest one to FES2004. The phase shift of the absolute value of acceleration between the models brings the acceleration differences in a wave form which is asymmetry both in form and value. In Fig.4.5 the absolute value of acceleration oscillate both with a high frequency as shown in Fig.4.4 and with superimposed low frequency which has a period of half month. In Fig. 4.6 we see that the acceleration differences are predominantly positive and sometimes exceeding 0.02 mGal. Moreover the acceleration difference between EOT08a and FES2004 is basically larger than between EOT10a and FES2004.

**Figure 4.5:** *Absolute value of accelerations at* $65° N \, 80° W$, *start time 00:00 UTC on 1st March, 2000*
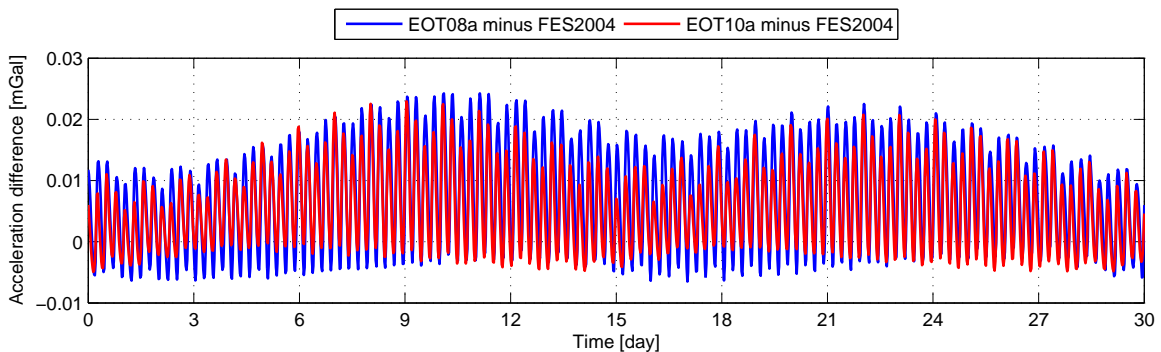
Figure 4.6: *Acceleration difference at* $65° N \, 80° W$, *start time 00:00 UTC on 1st March, 2000*

4.1.2 The St. Lawrence River Valley

The most tremendous model difference all over the world emerges at the St. Lawrence River Valley with the evidence that the potential difference of S2 between EOT10a and FES2004 nearly reaches 16 mm in geoid height. The St. Lawrence River connecting the Great Lakes with the Atlantic Ocean traverses the Canadian provinces of Quebec and Ontario and forms part of the international boundary. The coordinate 47°N 71°W of Quebec is chosen for the research in this area. It should be aware that the chosen place is on land and the acquired signals from river valley are normally very weak, which means that this area ought to be excluded from the model of ocean tides and show no potential difference between them. The comparison shows that the

model EOT10a has a shortage at the St. Lawrence River Valley. This is also proved through the personal communication with the producer of the EOT models (Savcenko and Bosch, 2008), that EOT10a performs not well at this location due to a poor observation.
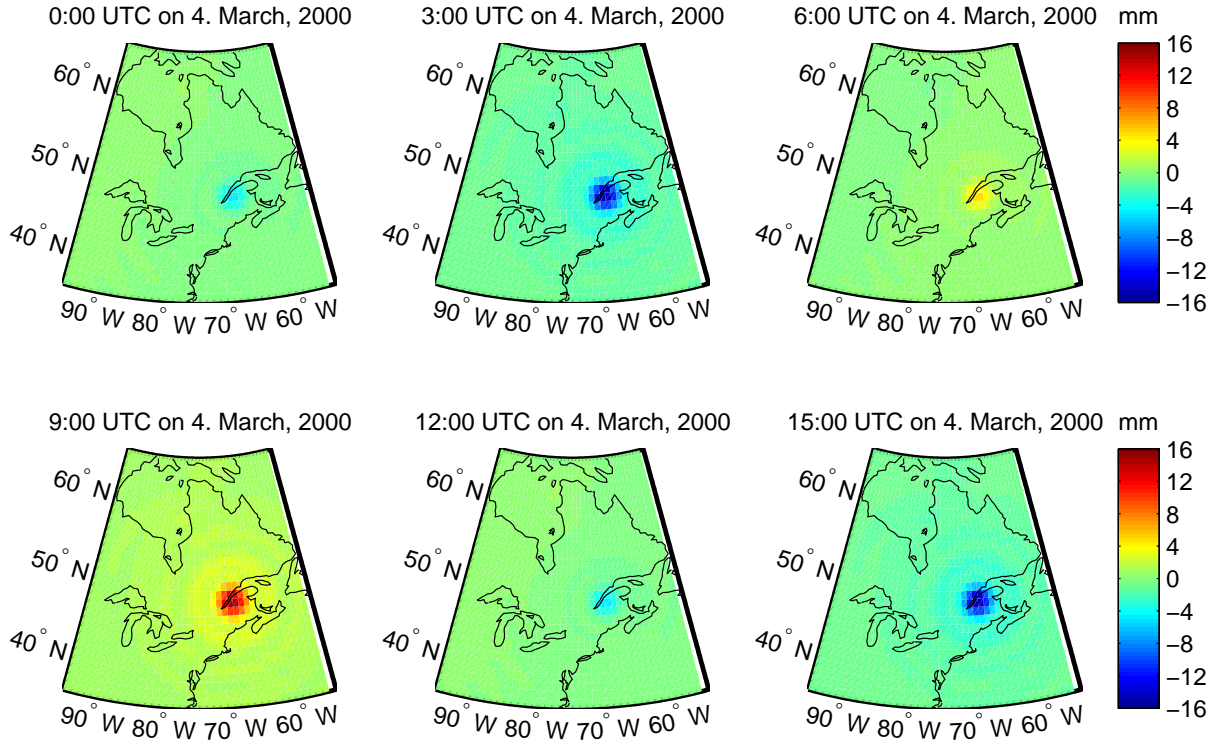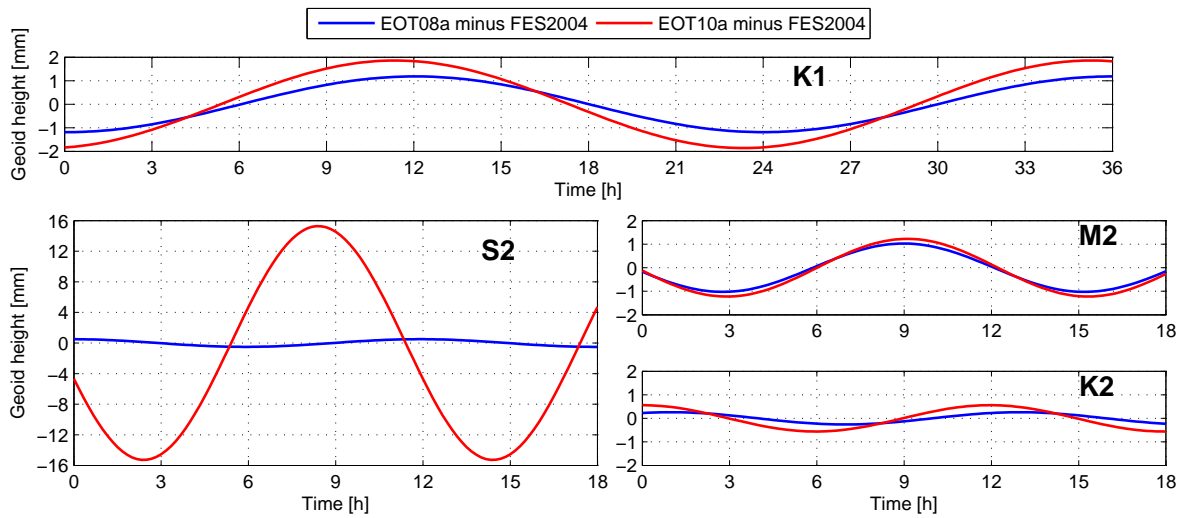

Figure 4.7: *Potential difference of S2 between EOT10a and FES2004 in geoid height, the St. Lawrence River Valley*

Fig. 4.7 illustrates the potential difference of S2 in this area at interval of 3 hours. These images coincide with the situation presented in the graphic of S2 in Fig. 4.8. Compared with Fig. 4.2, the order of the constituents S2 and M2 in Fig.4.8 are changed over, because not M2 but S2 has a more outstanding profile at the St. Lawrence River Valley. Although the tremendous potential difference of S2 tide between EOT10a and FES2004, EOT08a only differs from FES2004 for less than 1 mm in geoid height. The potential differences of the other major constituents are all less than 2 mm. Phase shift is not very evident.

The amplitude of the total potential difference between EOT10a and FES2004 from Fig. 4.9 shows that the model difference is dominated by S2, which suppress the contribution of other major constituents. Total potential difference between EOT08a and EOT10a is within 5 mm of geoid height and stays more often in the positive side than the negative side. The half month period are relative vague in Fig. 4.9 but can still be recognized.

In Fig. 4.10 we see that the left panel and right panel show very similar pattern which is dominated by FES2004. The curve from FES2004 and EOT08a overlap with each other and are both under 0.01 mGal. Therefore their difference forms a line almost with constant value of zero. The acceleration from EOT10a has a bell shape and repeats itself approximately every 6 hours with slight change in amplitude. The acceleration difference between EOT10a and FES2004 also forms a bell shape, because they have magnitude difference of factor 10.

**Figure 4.8:** *Potential difference of single constituent at* $47°N\,71°W$*, start time 00:00 UTC on 1st March, 2000*
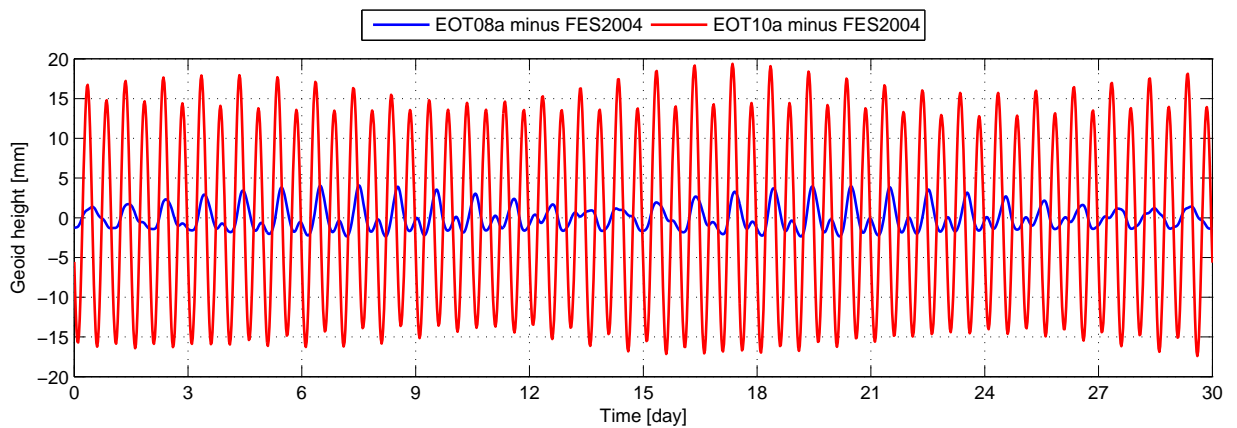
Figure 4.9: *Total potential difference at* $47°N\,71°W$*, start time 00:00 UTC on 1st March, 2000*
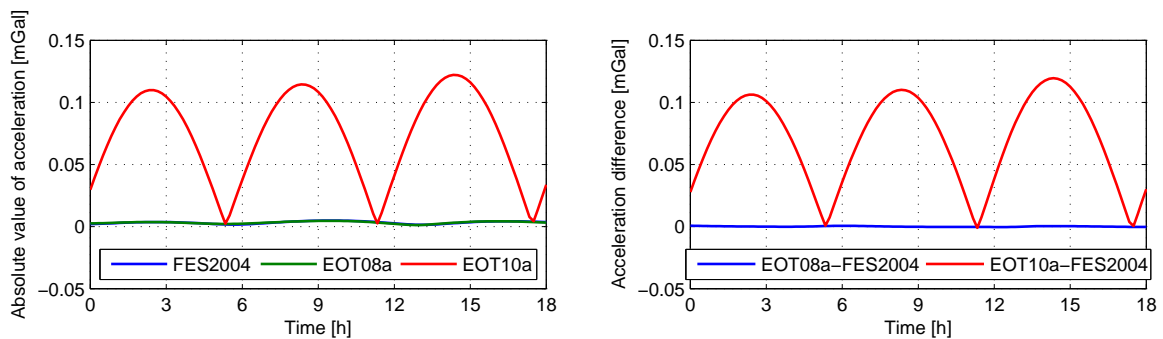
Figure 4.10: *Absolute value of acceleration and acceleration difference at* $47°N\,71°W$*, start time 00:00 UTC on 1st March, 2000*

The Similarity of acceleration value from FES2004 and EOT08a is also maintained in a long time period as showed in Fig. 4.11, in which the blue curve of FES2004 is totally covered by the green one. The graphic of acceleration difference in long time period, which is not presented here, looks very much the same as Fig. 4.11.
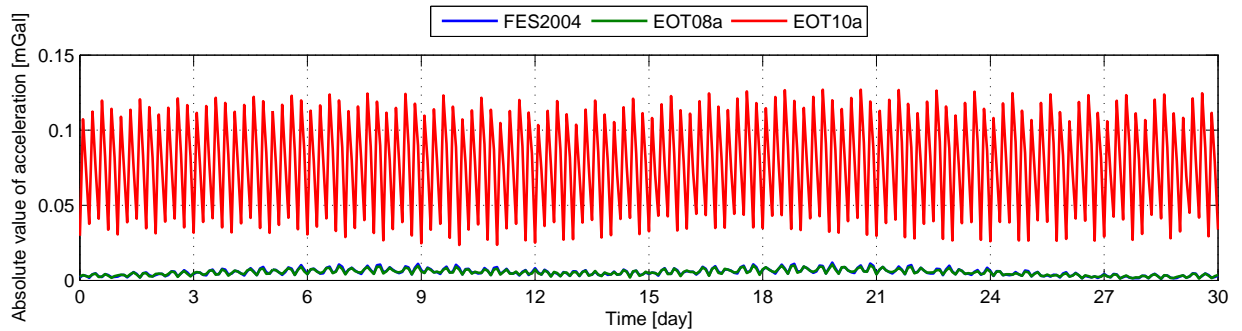

Figure 4.11: Acceleration difference at $47°N\,71°W$, start time 00:00 UTC on 1st March, 2000

4.2 The Patagonian Shelf and the South Pacific Ocean

It is a fact that the signals in Patagonian shelf and in deep oceans are quite strong (Savcenko and Bosch, 2008), so the ocean tide models must be very good at these areas. In this section one point in the Patagonian Shelf and one point in the middle of the South Pacific Ocean are chosen as examples to show the model difference in area with strong signals. These two examples demonstrate that both the EOT models do not significantly differ from each other but from FES2004.

4.2.1 The Patagonian Shelf
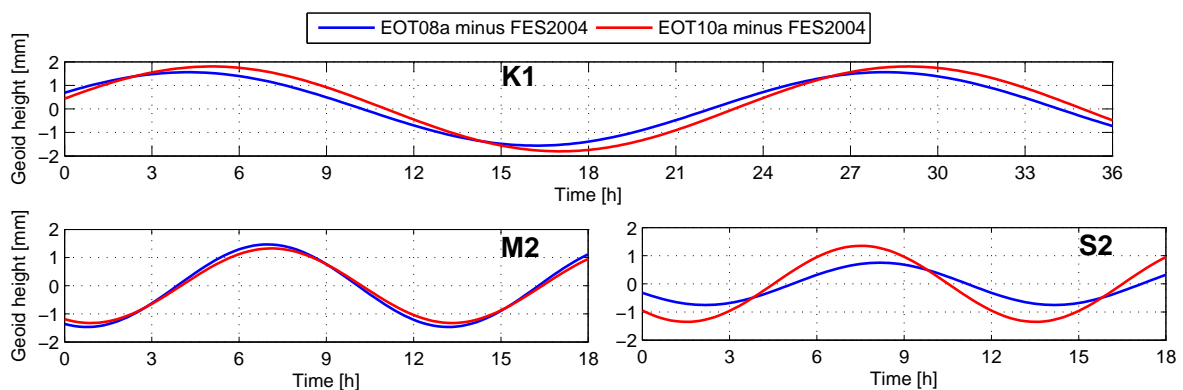
Figure 4.12: Potential difference of single constituent at $51°S\,64°W$, start time 00:00 UTC on 4. March, 2000

The Patagonian Shelf extends from Uruguay to the Strait of Magellan. It is relatively narrow in the North but widens progressively to the South, where the chosen point is located. Fig. 4.12 shows that the potential differences of K1, M2 and S2 between the two EOT models are quite

small and between the EOT models and FES2004 are significant but not more than 2 mm in geoid height. In the chart of S2 we see both amplitude difference and clear phase shif clearly. The total potential difference between the EOT models and FES2004 is no more than 7 mm in geoid height and show a periodic variation of amplitude in half month.
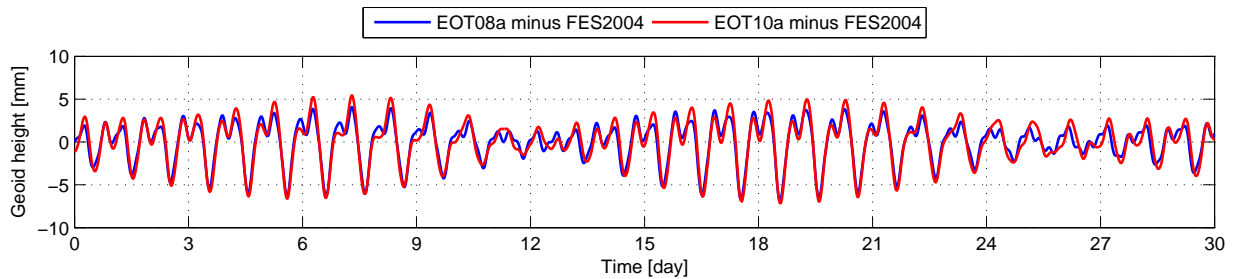

Figure 4.13: *Total potential difference at $51°S\ 64°W$, start time 00:00 UTC on 1. March, 2000*

Except the small difference in amplitude,the absolute values of acceleration of three investigated models coincide with each other pretty well. The amplitude in Fig.4.15 tells that EOT10a differs from FES2004 slightly less than EOT08a from FES2004 in regard to the absolute value of acceleration. The maximal absolute value of acceleration at this point exceed 0.10 mGal, however the acceleration differences between models are less than 0.01 mGal.
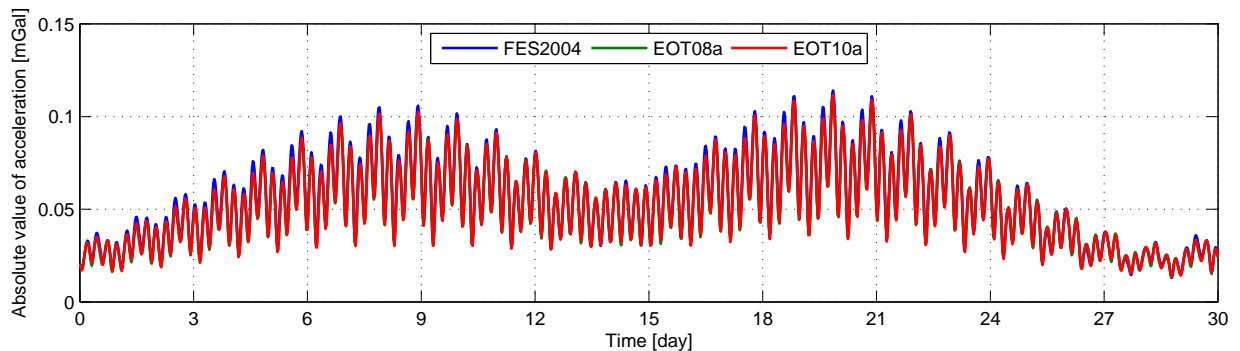
**Figure 4.14:** *Absolute value of acceleration at $51°S\ 64°W$, start time 00:00 UTC on 1. March, 2000*
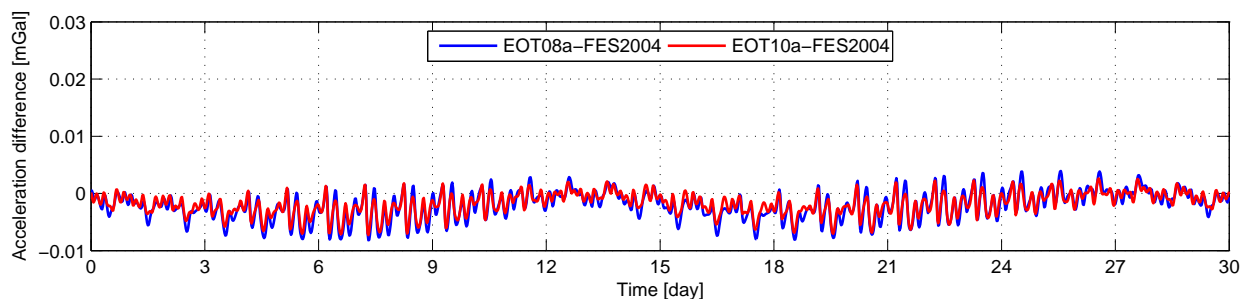
Figure 4.15: *Acceleration difference at $51°S\ 64°W$, start time 00:00 UTC on 1. March, 2000*

4.2.2 The South Pacific Ocean

The point 51°S 64°W in the middle of the South Pacific Ocean is taken as an example for deep oceans. The situation at this chosen point is alike the last example in many aspects. The potential difference between the two EOT models is quite small but between the EOT models and FES2004 it show difference in some extent.

The potential differences of S2 between the EOT models and FES2004 are less than 1 mm in geoid height and show again clear phase shift between the EOT models. EOT10a differs from FES2004 a little bit more than EOT08a does. The chart of K1 shows amplitudes and phase shift alike the situation of K1 in the other examples of chapter. The two curves of M2 coincide with each other perfectly, which means that the two EOT models are exactly the same at this place with respect to potential of M2. Compared with the other M2 chart previously, we notice that the y-axis of this M2 chart changes its scale, for the potential difference exceeds slightly 2mm in geoid height.
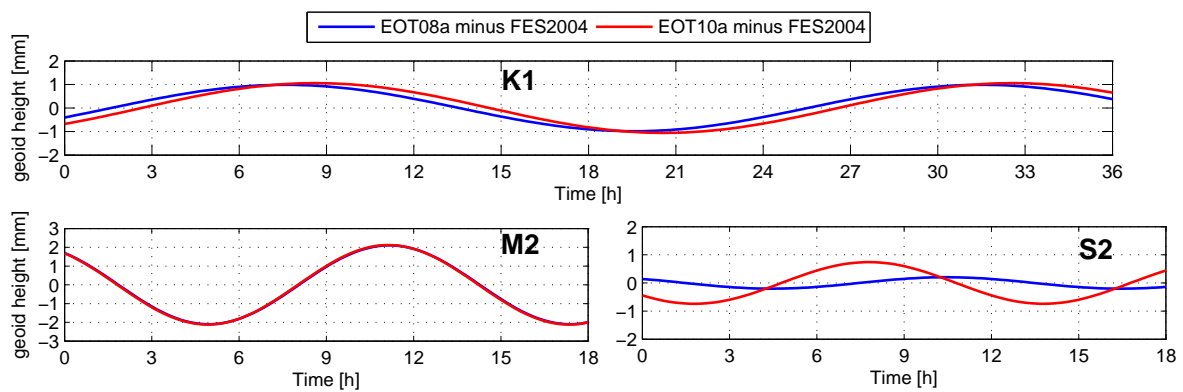
Figure 4.16: *Potential difference of single constituent* $30°S\,120°W$, *start time 00:00 UTC on 4. March, 2000*

The total potential difference between the EOT models and FES2004 is no more than 5 mm in geoid height and a periodic variation of amplitude in half month is not very pronounced. As stated above, the two curves coincide with each other well, because of the resemblance of the EOT models at this chosen place.
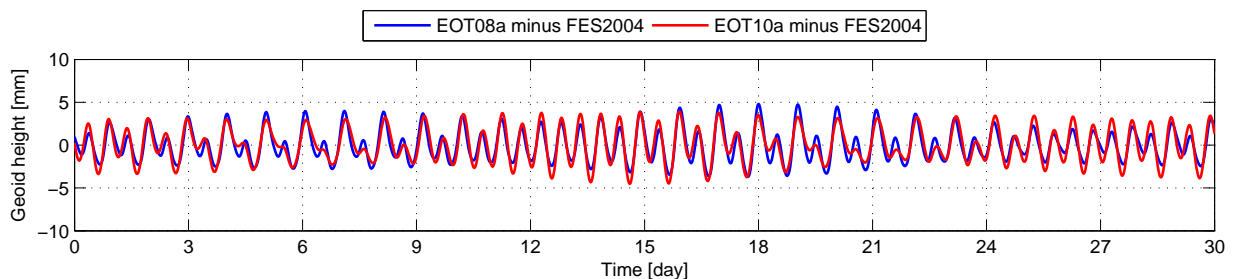

**Figure 4.17:** *Total potential difference at* $30°S\,120°W$, *start time 00:00 UTC on 1. March, 2000*

In all these three models, the ocean tides have an influence on the acceleration at the observation point far below 0.05 mGal. Since the three lines overlap in Fig. 4.18, only the red line representing EOT10a on the top can be seen. That means the tide models have almost the same absolute

value of acceleration at this point in the middle of the deep ocean. If we pay attention to the scale of y-axis in Fig. 4.19 that illustrates the value difference, we know that the value differences is factor 10 smaller than the absolute value of accelerations and the EOT models have exactly the same value of acceleration here.
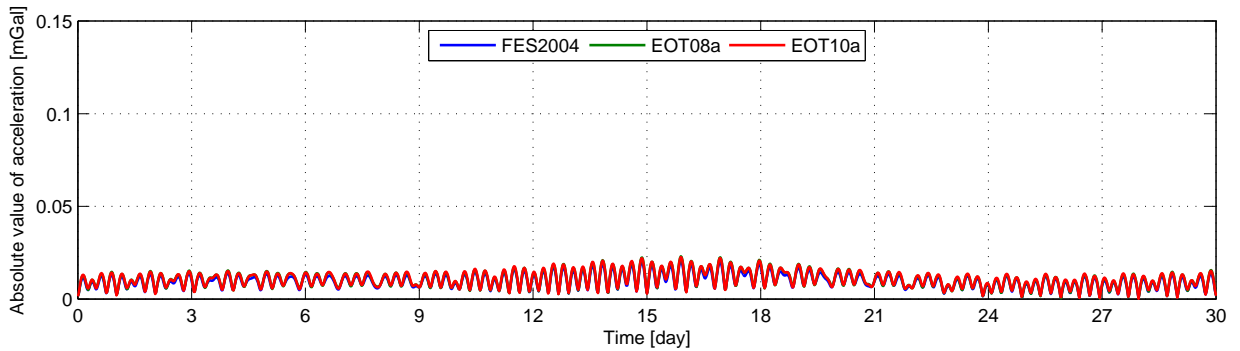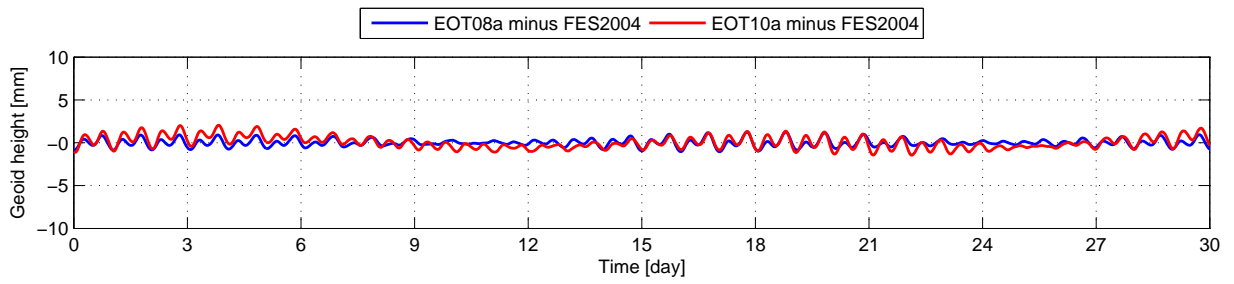

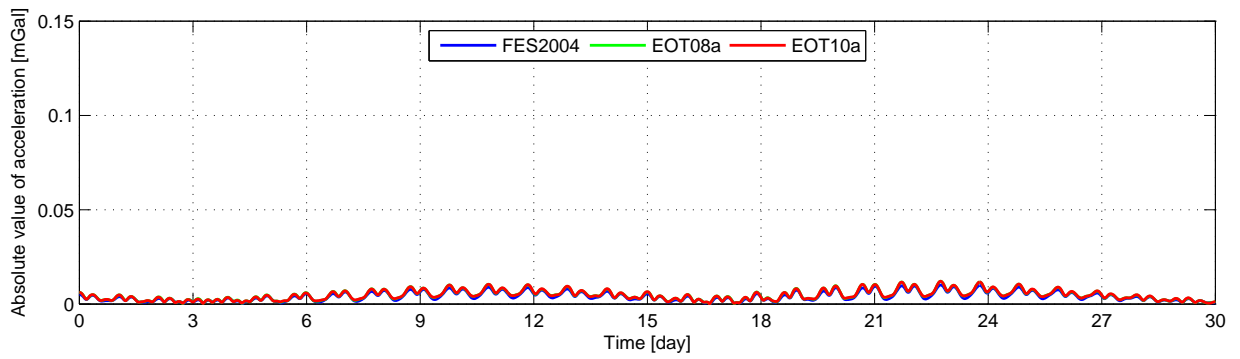**Figure 4.18:** *Absolute value of acceleration at $30°S$ $120°W$, start time 00:00 UTC on 1. March, 2000*
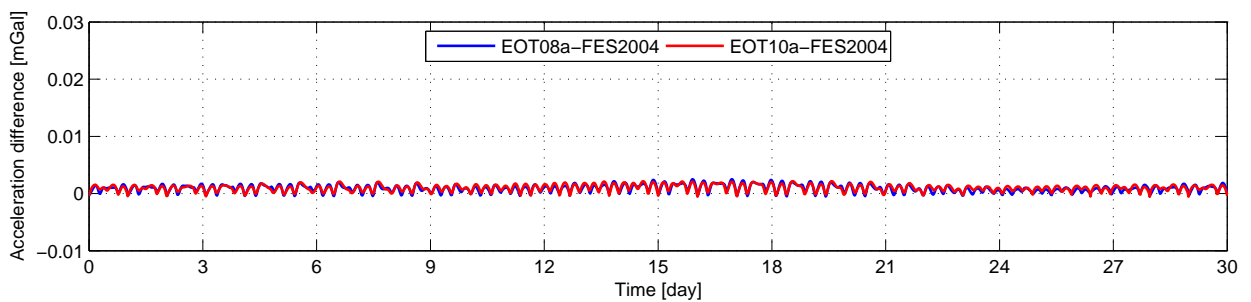
Figure 4.19: *Acceleration difference at $30°S$ $120°W$, start time 00:00 UTC on 1. March, 2000*

4.3 The Arctic and the Antarctic

The vast land of the Antarctic is covered by permanent ice sheet as well as most of the Arctic. There should be no signal or at least very weak signals for measurements in those areas, as the water is not in liquid state. Theoretically no model difference or very little difference should be fund in these regions. Fig 4.20 and Fig 4.21 present the total potential difference between the models and the absolute value of acceleration of each model at one location in the middle of Antarctic.

Figure 4.20: *Total potential difference at* $78° S \ 44° W$, *start time 00:00 UTC on 1. March 2000*

Figure 4.21: *Absolute value of acceleration at* $78° S \ 44° W$, *start time 00:00 UTC on 1. March 2000*

Chapter 5

Spherical harmonic analysis of GRACE observations under the influence of ocean tide model errors

5.1 Adaptation to GRACE satellites

Based on the knowledge introduced in Section 2.5, two Matlab scripts haven been written for the two tasks in this chapter. One of them is called SIMULATOR, which performs the orbit simulation of the twin GRACE satellites. The other one is named SIMSOLVER that carries out the spherical harmonic analysis by using the output datasets from SIMULATOR as input information. These two scripts contribute to form a closed loop simulation where influences of errors can be evaluated by comparing the input and output models. It will be explained in the later part of this section.

The numerical information of GRACE satellites from the University of Bonn (Ilk et al., 2005) is adopted to build the simulator. Except for the difference in launch time of 30 seconds, the two satellites share the same value for the orbit parameters, namely five of the six Keplerian elements.

	GRACE 1	GRACE 2
t_0: launch time [dd mm yy hh min sec]	15 07 2000 00 00 00	15 07 2000 00 00 30
a: Semi-major axis [km]	6778	6778
e: Eccentricity	0.001	0.001
i: Inclination [rad]	1.562069681	1.562069681
Ω: Longitude of the ascending node [rad]	0	0
ω: Argument of perigee [rad]	0	0

Table 5.1: *The initial values of GRACE*

SIMULATOR generates data sets in an arbitrary time period described by time series t which are defined by start and end time and time step. The input data also includes the two ocean tide models that are going to be compared and the maximum degree of the spherical harmonic expansion. After each execution, SIMULATOR outputs data for the two GRACE satellites, the GAST angle and the time series t in the form of modified Julian day. The data for each satellite contains the items listed in Tab. 5.2.

Item	Reference system	Coordinate system	Data Type
Position $\mathbf{x}_i$	Inertial	Cartesian	vector
Speed $\mathbf{v}_i$	Inertial	Cartesian	vector
Position $\mathbf{x}_e$	Earth-fixed	Spherical	vector
Disturbance in the acceleration $\mathbf{a}_1$	Earth-fixed	Cartesian	vector
Disturbance in the acceleration $\mathbf{a}_2$	Earth-fixed	Cartesian	vector
Signal $\mathbf{f}$	Earth-fixed	Cartesian	vector

Table 5.2: *The output of simulator for the twin GRACE satellites*

The disturbance in the acceleration $\mathbf{a}$ in Tab. 5.2 is the accelerations due to ocean tides along the satellite orbit at the desired time stamps. The numerical subscripts indicate the correspondence to the two input ocean tide models. Besides the acceleration of this kind, the accelerations due to Earth gravity field $\mathbf{g}$ is also simulated along the orbit. The simulated signal $\mathbf{f}$ listed in Tab 5.2 is generated by Eq. 5.1.

$$\mathbf{f} = \mathbf{g} + \mathbf{a}_1 - \mathbf{a}_2 \tag{5.1}$$

SIMSOLVER performs spherical harmonic analysis for the signal $\mathbf{f}$. The subscripts A and B in Section 2.5.2 correspond to the first and the second GRACE satellites. The term ∇V_A and ∇V_B in Eq. 2.33 are in this case specified to the simulated signal $\mathbf{f}$ for the two GRACE satellites respectively. The simulation scenarios are simplified in such a way as there is no noise on the data for the GRACE observable. SIMSOLVER yields besides the spherical harmonic coefficients also its formal errors and if requested the standard deviation. Currently the solver does not handle any error information, i.e. the pseudo-observations are assumed equally precise.
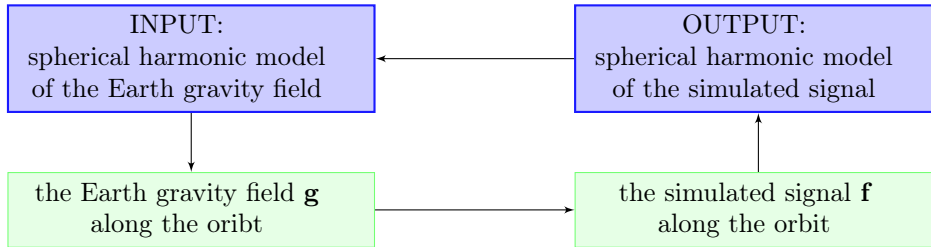

Figure 5.1: *Flow chart of the closed loop simulation*

Fig. 5.1 demonstrates the principle of the closed loop simulation mentioned at the beginning of this section. As input, we have a data set of the spherical harmonic coefficients of the Earth gravity field model. Based on it, the simulated signal $\mathbf{f}$ can be computed as described in the previous paragraphs. The difference between $\mathbf{f}$ and $\mathbf{g}$ is exactly the acceleration difference derived from two tidal models. Since none of the ocean tide models is 100 percent correct, without knowing the truth, there is no way to judge which model is absolutely better than the others. Conventionally, a certain percentage of the model difference is regarded as error. Thus, the signal $\mathbf{f}$ can be interpreted as the Earth gravity field under the influence of ocean tide modal errors. The spherical harmonic coefficients derived from it, with the help of SIMSOLVER, are faulted coefficients. Through the comparison of the two spherical harmonic coefficients sets, the influence of ocean tide model errors on GRACE observation is demonstrated.

In other words, the results of this closed loop simulation shows the difference of ocean tides modeling in frequency domain. The difference appears mainly on the coefficients of lower degree. Among those coefficients, the zonal spherical harmonics in odd degree are prominent. The largest model difference (error) appears at the coefficient of degree 0 that describes the mass of the Earth. Since GRACE observations are not sensitive to degree 0 at all, this must be an error in the modeling. Further, it is found that the energy of the model errors distributes on certain frequency, which are usually the natural frequency or its multiple of the GRACE satellites. This phenomenon is mainly due to the time aliasing problem of GRACE.

5.2 Application examples

It is mentioned in Section 2.5.2 that the successful performance of the least squares adjustment requires not only adequate observation redundancy, but also observations homogeneously covering the Earth surface. For the example in this section, the time period from 1. Aug. 2010 at 0 o'clock to 31. Aug. 2010 at 24 o'clock with time step of 5 s is chosen as the input time series. Illustrated in Fig. 5.2 is the regional ground track plot of the first GRACE satellite for this time period, during which the GRACE satellites cover the Earth fully. To achieve a better visual presentation, the foot prints in Fig. 5.2 have a time interval of 1 min and are limited by the longitude.
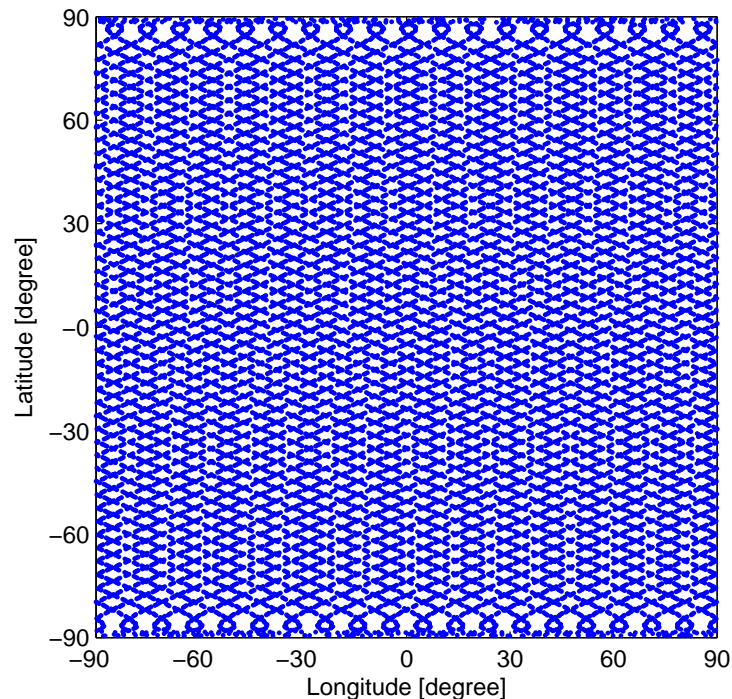

Figure 5.2: *Regional ground track plot of the first GRACE satellite,from 0:00 on 1. Aug. 2001 to 0:00 on 1. Sep. 2001*

The two ocean tide models as input of SIMULATOR are ETO08a and FES2004 or EOT10a and FES2004 in each case. To compute the Earth gravity field, we use the model named itg_grace2010s (Mayer-Guerr et al., 2010). The maximum degree of the spherical harmonic

expansion for the calculation is set as 50 and 100 respectively. This value can actually be any integer number less than 180, because the adopted static gravity field model `itg_grace2010s` is limited to degree 180. Although ocean tide models do not reach high degree like 100, it is still interesting to find out what does the result looks like.

The output data of `SIMULATOR` are further provided to `SIMSOLVER`. The maximum degree of the spherical harmonic expansion for signal $\mathbf{f}$, as one of the input parameters of `SIMSOLVER`, is consistent to the case for `SIMLATOR`, either 50 or 100. The numerical results of this example shown in Fig. 5.3 are actually the difference of the spherical harmonic coefficients

$$\overline{C}_{lm}(\mathbf{f}) - \overline{C}_{lm}(\mathbf{g}) \quad \text{and} \quad \overline{S}_{lm}(\mathbf{f}) - \overline{S}_{lm}(\mathbf{g})$$
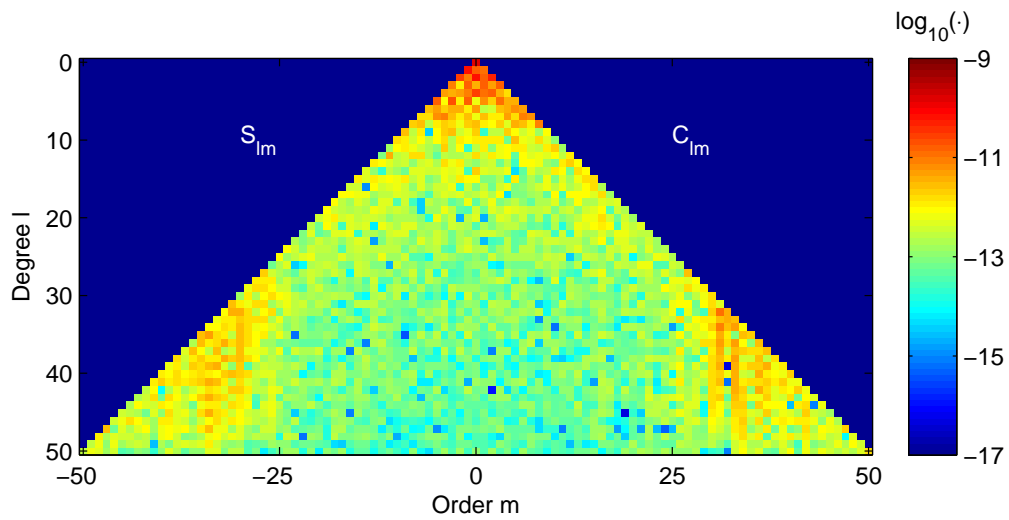

(a) Aug.2010, EOT08a - FES2004, maximum degree L=50
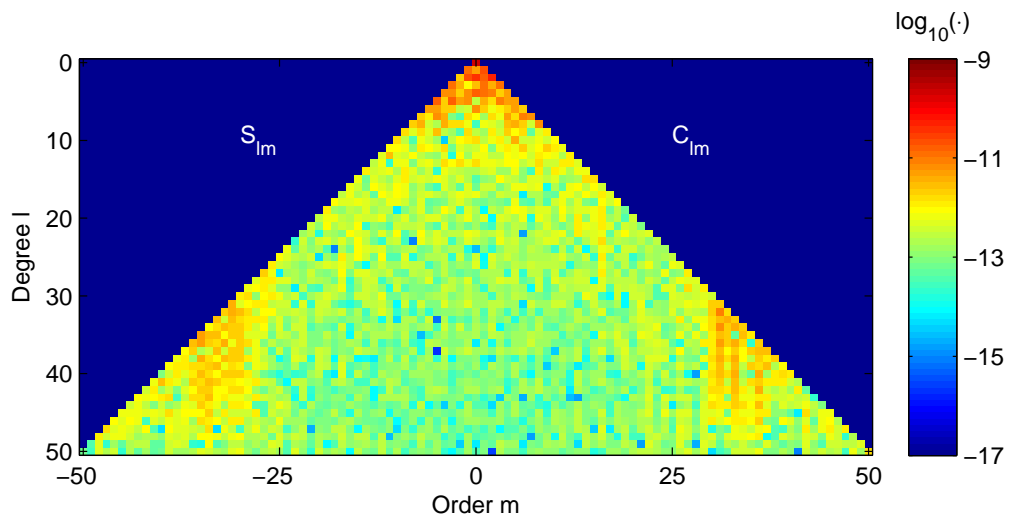
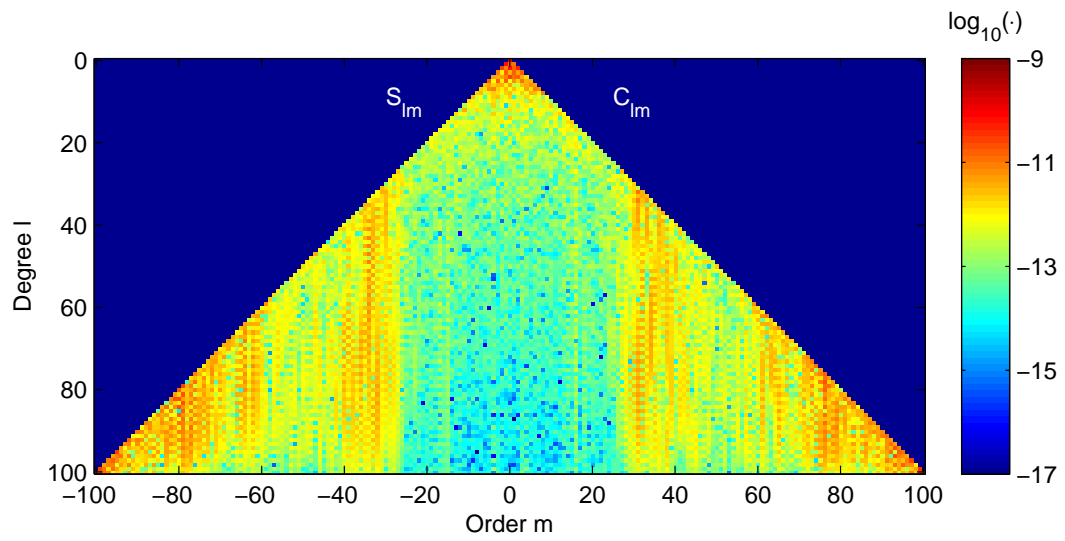(b) Aug.2010, EOT10a - FES2004, maximum degree L=50

Figure 5.3: *Impact of difference between ocean tide models on GRACE satellites interpreted in form of spherical harmonic coefficients*

In spite of the resemblance of image (a) and (b) of Fig. 5.3, it can be recognized that the red and orange color in image (b) is less than that in image (a), which means that EOT10a resembles FES2004 more than EOT08a does. In both images, the grids with red and orange color gather dominantly on the head of the coefficient triangle, namely in the area of low degree and order. The maximum in both images appears at the coefficient in degree 0 order 0, according to Fig. 5.4, which demonstrates the numeric information of the coefficients with degree lower than 8 in image (a) and (b) of Fig. 5.3. As the statistical proof of the first sentence in this paragraph, it is seen clearly that except the degree 0, the values from image (b) are smaller than that from image (a). The other two patches of the warm color in Fig. 5.3 locate symmetrically at the waist of the coefficient triangle showing strip patterns between order 30 and 34. This phenomenon is demonstrated more clearly and strongly in Fig. 5.5, in which the maximum degree of the spherical harmonic expansion is 100.
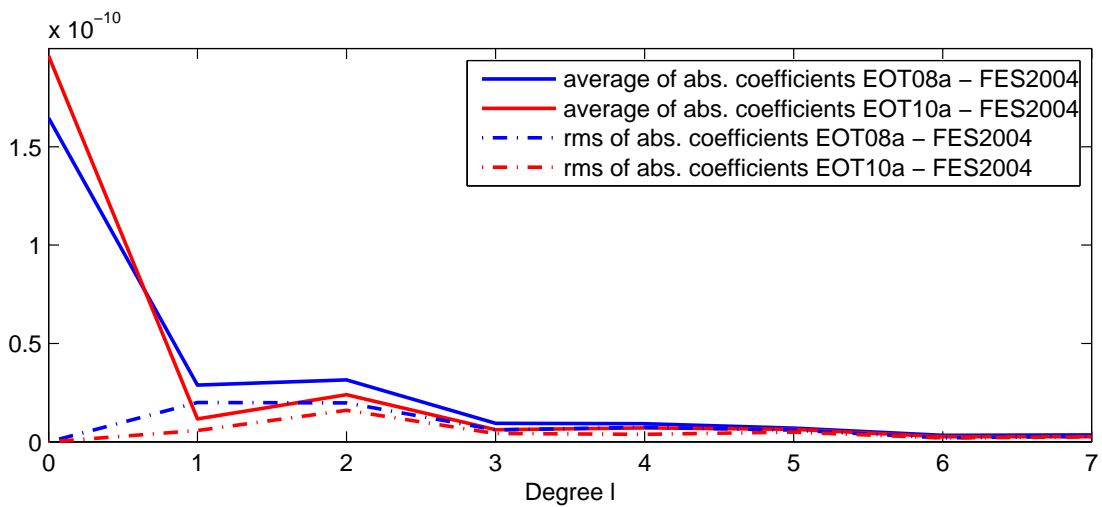

Figure 5.4: *Average and rms of the coefficients of a certain degree in image (a) and (b) of Fig. 5.3*

Therefore, the strip patterns at certain order in Fig. 5.5 can be interpreted as the energy of the error distributes on certain frequency, which are usually the natural frequency or the multiple of it. For example, there are two symmetrical yellow strips in order 16, which are not very distinct but still visible, especially in the image (a). This is also the natural frequency of the GRACE satellites, since they circle the Earth 16 times a day. Further, apparently there are strips in near the oder 32, whose absolute value is the double of 16. This phenomenon is mainly due to the time aliasing problem of GRACE.

(a) Aug.2010, EOT08a - FES2004, maximum degree L=100
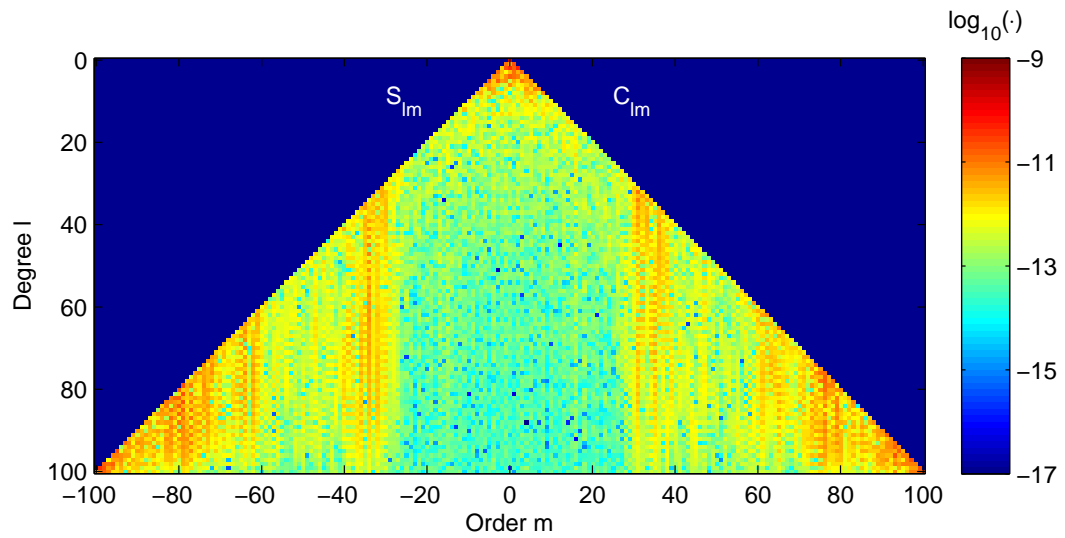
(b) Aug.2010, EOT10a - FES2004, maximum degree L=100

Figure 5.5: *Impact of difference between ocean tide models on GRACE satellites interpreted in form of spherical harmonic coefficients*

At the end of this numerical example, a transformation from the frequency domain to the spatial domain is performed. Based on the spherical harmonic coefficients, which are developed from the spherical harmonic analysis with the max. degree of 50, potential field on the Earth surface with the height of 6378146 m are calculated and presented in terms of geoid height. According to the calculation result, the simulations have a system bias of -0.6083 mm. After subtracting the bias, the potential field is shown as in Fig. 5.6.
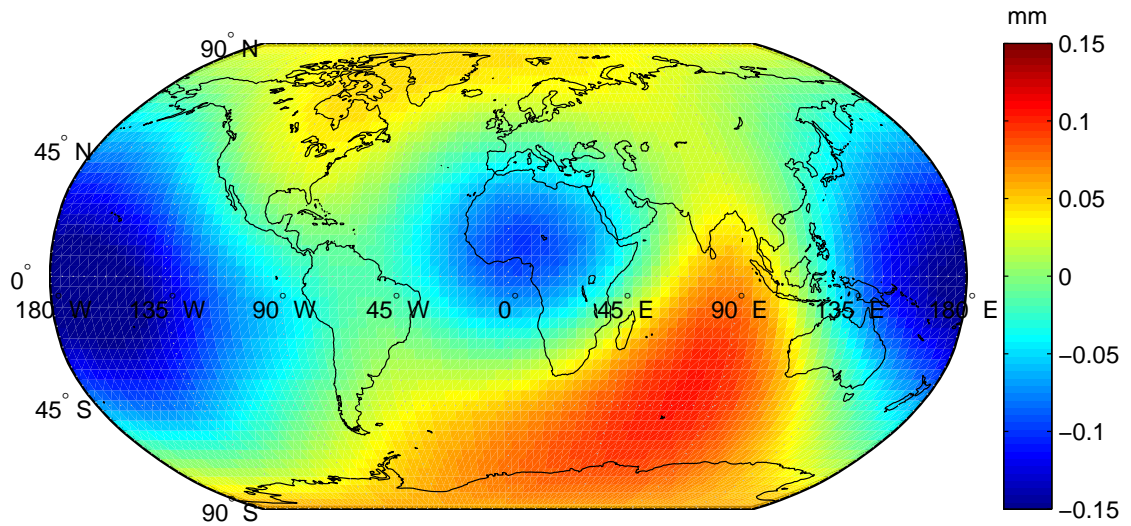
Figure 5.6: *Presentation of the coefficient difference in Fig. 5.3 in spatial domain in terms of geoid height*

Chapter 6

Conclusion

Based on the given tidal maps from ocean tides model FES2004, EOT08a and EOT10a, the disturbance in the potential due to ocean tides is successfully computed on the Earth surface for each model. By using the global visualization tool and the local visualization tool developed in this thesis, it is found that S2 and M2 tide are the tides that dominate the potential difference between the EOT models and FES2004. EOT08a shows distinct potential difference to FES2004 for M2 tide at the Foxe Basin with the maximum of about 4 mm in terms of geoid height. EOT10a makes improvement in this case that it reduces potential difference to FES2004 to approximately 1 mm in terms of geoid height. However, it shows a tremendous potential difference against FES2004, almost 16 mm in terms of geoid height, for the S2 tide at the St. Lawrence River, which is proved as model error (Savcenko and Bosch, 2008) for the S2 tide. Except the case at the St. Lawrence River, for S2 tide in general, EOT08a has a little less potential difference to FES2004 than EOT08a does. The difference between the EOT models is distinctly smaller than the difference between the EOT models and FES2004. The periodogram of the potential difference between the models tells that, besides amplitude, the EOT models also differ from each other slightly in terms of phase.

The orbit simulation enables the presentation of the potential difference between the models along the orbit of GRACE satellites. The spherical harmonic analysis shows that the potential differences reflect mainly on the coefficients of lower degree which is not lager than 6. Except the spherical harmonic coefficient of degree 0, which is inferred as an error in the modeling, the other coefficients of the lower degree show that EOT10a resembles FES2004 more than EOT08a does. Due to the time aliasing problem of GRACE, potential difference between models also reflect on the coefficients of the order 16, which coincides to the natural frequency of GRACE satellites, and its multiple.

As ocean tide model EOT11a is already available, the comparison of EOT11a and FES2004 can be done in the future, based on which we can find out the improvement in EOT11a against EOT08a and EOT10a.

Bibliography

Balmino, G. (1995), Ellipsoidal corrections to spherical harmonics of surface phenomena gravitational effects.

Casotto, S. (1989), Nominal ocean tide models for TOPEX precise orbit determination, PhD thesis, The University of Texas at Austin.

Doodson, A. (1921), 'The harmonic development of the tide-generating potential', **100**(704). Proceedings of the Royal Society of London. Series A, Containing Papers of a Mathematical and Physical Character.

Dow, J. (1988), 'Ocean tides and tectonic plate motions from Lageos'. Bayerische Akademie der Wissenschaften. Geodaetische Kommission, Reihe C, Heft Nr. 344.

Ilk, K. H., Mayer-Guerr, T. and Feuchtinger, M. (2005), Gravity Field Recovery by Analysis of Short Arcs of CHAMP, Technical report.

Marsh, J. G., Lerch, F. J., Christodoulidis, D. C., Putney, B. H., Felsentreger, T. L., Sanchez, B. V., Smith, D. E., Klosko, S. M., Martin, T. V. and Pavlis, E. C. (1987), An improved model of the earth's gravitational field: GEM-T1, Technical report, Goddard Space Flight Center.

Mayer-Guerr, T., Kurtenbach, E. and Eicker, A. (2010), ITG-Grace2010:the new GRACE gravity field release computed in Bonn. EGU General Assembly 2010, held 2-7 May, 2010 in Vienna, Austria.

Savcenko, R. and Bosch, W. (2008), EOT08a - empirical ocean tide model from multimission satellite altimetry, Technical Report 81, Deutsches Geodaetisches Forschungsinstitut (DGFI).

Simon, J. L., Bretagnon, P., Chapront, J., Chapront-Touze, M., Francou, G. and Laskar, J. (1994), 'Numerical expressions for precession formulaeand mean elements for the Moon and the planets', *Astronomy and Astrophysics* **282**(2), 663–683.

Appendix A

List of the places studied in Chapter 4 with coordinates of longitude and latitude.

1. the Atlantic Ocean northeast of the United States 38°N 74°W
2. the Pacific Ocean southwest of the United States 35°N 126°W
3. the Foxe Basin 65°N 80°W
4. the Hudson Bay 60°N 85°W
5. the St. Lawrence River Valley 47°N 71°W
6. the Great Lake 45°N 83°W
7. the Gulf of Mexico 24°N 90°W
8. the Patagonian shelf 51°S 64°W
9. the Gulf of Alaska 57°N 145°W
10. the Oklotsk Sea 57°N 143°E
11. the Yellow Sea 35°N 121°E
12. the South China Sea 13°N 114°E
13. the Bay of Bengal 15°N 87°E
14. the Arafura Sea 7°S 135°E
15. the Arabian Sea 16°N 64°E
16. the Indian Ocean 26°S 75°E
17. the South Pacific Ocean 30°S 120°W
18. the South Atlantic Ocean 27°S 14°W
19. the North Atlantic Ocean 33°N 36°W
20. the Antarctica 75°S 72°W
21. the North Pacific Ocean 28°N 165°E
22. the Mediterranean Sea 40°N 5°E
23. the North Sea 54°N 2°E
24. the Baltic Sea 55°N 17°E
25. the Bay of Biscay 45°N 4°W
26. the Celtic Sea 49°N 7°W
27. the Arctic Ocean 80°N 141°W
28. the Northwestern Passages 68°N 101°W
29. the Weddell Sea 74°S 44°W
30. the Ross Sea 76°S 173°W